



Regional resource assessment and geothermal models

D 3.4

Regional resource assessment and geothermal models

D 3.4

Final version

Damien Bonté, Jon Limberger, Eugenio Trumpy,
Gianluca Gola, Jan Diederik van Wees

Work package 3

29 03 2019



This report is freely available under the Creative Commons Attribution International 4.0 Licence (CC BY 4.0)

Website: <http://www.gemex-h2020.eu>



The GEMex project is supported by the European Union's Horizon 2020 programme for Research and Innovation under grant agreement No 727550

Table of Contents¹

List of figures	4
List of tables	5
Executive summary	7
1 Introduction	8
1.1 <i>Los Humeros geological framework</i>	8
1.2 <i>Acoculco geological framework</i>	10
2 Regional temperature structure of Los Humeros	12
2.1 <i>Data</i>	12
2.1.1 Temperature	12
2.1.2 Geological model	15
2.1.3 Hydrogeology	16
2.2 <i>Methodology</i>	17
2.2.1 Model geometry and thermal properties	17
2.2.2 Forward model	20
2.2.3 Magmatism	21
2.2.4 Hydrothermal fluxes	21
2.3 <i>Model results</i>	24
2.3.1 Magmatism results	25
2.3.2 Magmatism combined with regional groundwater fluxes	27
3 Regional temperature structure of Acoculco	31
3.1 <i>Data</i>	31
3.1.1 Temperature	31
3.1.2 Geological model	33
3.2 <i>Methodology</i>	33
3.3 <i>Result of the thermal model</i>	36
4 Resource assessment	37
4.1 <i>Methodology</i>	37
4.2 <i>Resource assessment results for Los Humeros</i>	38
4.3 <i>Resource assessment results for Acoculco</i>	40
5 Conclusion	43
6 References	44

¹ The content of this report reflects only the authors' view. The Innovation and Networks Executive Agency (INEA) is not responsible for any use that may be made of the information it contains.

List of figures

Figure 1: Location of Los Humeros caldera and geothermal field. a) Inset map showing the distribution in the eastern Trans Mexican Volcanic Belt (TMVB). b) Digital Elevation Model for Los Humeros showing the main structural features (Los Potreros and Los Humeros scarps) – from Carrasco-Núñez et al. (2017).....	8
Figure 2: Geological map of Los Humeros adapted from Carrasco-Núñez et al. (2017)	10
Figure 3: examples of temperature log in the well H-43. Left: time series within the day after drilling. Right: 20 days recovery and dynamic measurement.	12
Figure 4: BHT temperatures in Los Humeros. Left: Time series BHT corrected using the ICS method. Right: Higher (and therefore deeper) temperature recoded on the logs with few weeks recovery.	13
Figure 5: Thermal gradient from the equilibrium BHT temperature in the wells in Los Humeros	14
Figure 6: Humeros regional geological model including the fault model (see 3DLHRegionalFaultModel) and the four geological groups listed at bottom left. AA': Carrasco-Núñez et al. (2017a) cross-section, BB': Norini et al. (2015) cross-section. Source Calcagno et al., 2018.	15
Figure 7: Los Humeros watershed (source: T. Kretzschmar)	16
Figure 8: Inflow and Outflow for the Los Humeros	17
Figure 9: The parameterized model consisting of five main layers: three layers (1-3) correspond directly the groups G1-G3 (Table 1.1). Layer 4 corresponds to the top formations from the G4 group. Layer 5 corresponds to the bottom formation granitic crustal basement G4.....	19
Figure 10: (top) Hydrothermal boundary conditions of recharge (at the sides of the model, q_r) and discharge (at the caldera q_d). (bottom) Schematic section of the recharge and discharge boundary conditions and the simplified hydrogeological model to calculate the 3D flow field (with Eq. 2.4). The resulting flow field is used as v in (eq. 2.3).....	22
Figure 11: N-S and W-E cross sections through the steady-state conductive thermal field.	24
Figure 12: N-S and W-E cross sections through the thermal model based on the mean calculated temperatures after stochastically varying the emplacement depth of the heat source. (a) For the top model (model A in Table 3), wells H5, H14, H25 were used for calibration. (b) For the bottom model (model B in Table 3), all available wells were used, resulting in a shallower heat source.	26
Figure 13: Cross plots of observed and modeled temperature with depth of the measurements (top) and rank plots of modeled temperature (lines) and observed temperatures (dots) at the well locations, ranked by the modeled P50 values of temperature at the well locations. On the left, model A (a and c) and on the right, model B (b and d). ...	27
Figure 14: N-S and W-E cross sections through the thermal model based on the mean calculated temperatures after stochastically varying the hydro fluxes. (a) For the top model (model D, Table 3), the emplacement depth of the heat source was set at 5 km below sea level, while the thickness of the hydraulically conductive layer was increased to 5 km. (b) For the bottom model, the emplacement depth of the heat source was set at 2.5 km below sea level, while the thickness of the hydraulically conductive layer was kept at 1 km.....	29
Figure 15: Cross plots of observed and modeled temperature with depth of the measurements (top) and rank plots of modeled temperature (lines) and observed temperatures (dots) at the well locations, ranked by the modeled P50 values of temperature at the well locations (middle). At the bottom misfit (observed minus modeled temperatures).	

Red colors show a model overestimation of the temperature at the well location, while blue colors show and underestimation. On the left, model D (a, c, and e) and on the right, model E (b, d, and f).	30
Figure 16: Static temperature profiles with error bars (black dots and bars) of EAC-1 (left) and EAC-2 (right) wells. In EAC-1 well the two deepest temperatures came from the application of the Horner method to 2 time-temperature couples measured after 288 and 312 hrs since the circulation of the drilling mud stops.	32
Figure 17: The Acocolco regional geomodel of the five geological groups listed at bottom. Coordinate system is WGS84/UTM zone 14N. Figure taken from Calcagno et al. (2018).	33
Figure 18: Thermal profiles evaluated as soon as the intrusion starts to cool for an initial emplacement temperature of 850°C and its top set at 2300 m b.g.l.	37
Figure 19: Assessment of the geothermal potential from Limberger et al. (2014). For the Los Humeros and Acocolcu fields, the assessment was limited to the Theoretical Capacity (in red). Where H is the heat in place (J), V_{rock} is the rock volume (m^3), ρ_{rock} is the rock density (kg/m^3), $C_{p,rock}$ is the specific heat capacity of the rock (J/kg K), T_z is the temperature at depth z (°C), and T_r is the re-injection temperature (°C).	38
Figure 20: (a) Bottom view looking in NW-direction of the model cells with a calculated heat-in-place H larger than 10 PJ. (b) Stacked heat-in-place potential H normalized for cell surface area (PJ/km^2), showing the spatial distribution of H and major caldera faults. Most of the potential is associated with the high temperatures inside the caldera. The potential in the SE-corner can be explained by the thermal blanketing effect caused by the relative thick cover of layer 1 and 2 rocks with a very low (<2 W/(mK)) bulk thermal conductivity.	39
Figure 21: a) top limestone surface; b) top basement surface.	40
Figure 22: a) cross-section representing the volume of limestones where the HIP was computed; b) HIP map. Large red limit is the regional model boundary. Small red limit is the local geological model boundary. In black the trace of the cross-section reported in the part a of the Figure.	41
Figure 23: a) cross-section representing the volume of granite where the HIP was computed; b) HIP map. Large red limit is the regional model boundary. Small red limit is the local geological model boundary. In black the trace of the cross-section reported in the part a of the Figure X.	42
Figure 24: HIP map computed on Limestone plus Granite reservoir. Large red limit is the regional model boundary. Small red limit is the local geological model boundary.	43

List of tables

Table 1.1: Description of the geological formations in Los Humeros gathered into four groups and nine units (Calcagno et al., 2018).	9
Table 2.1: Temperature values gathered from the wells in Los Humeros	14
Table 2.2: Layer lithology.	18
Table 2.3: Lithology and thermal properties.	19
Table 2.4: Parameter variation for the different models. All models were run with 4 iterations ($N_a = 4$) with 200 model realizations ($N_e = 200$).	25

Table 3.1: Physical parameters of the lithothermal units	35
Table 3.2: Constitutive laws used to describe the macroscopic behaviour of the water-rock system	36
Table 4.1: Petrophysics used values in ThermoGIS runs.....	40

Executive summary

Both Acoculco and Los Humeros belong to the CFE (Comision Federal de Electricidad) under licencing for geothermal purposes. Los Humeros is a well-developed site with 65 wells drilled and has been producing electricity from Geothermal energy since 1991 and currently has an installed capacity of 94 MW. Los Humeros has been selected to be investigated in GEMex as a Super Hot Geothermal System (SHGS) with temperatures recorded in excess of 380°C. Acoculco is at the exploration stage with two wells drilled close to each other in 1994 and 2008. The system is dry with no major fluid circulation identified so far but with a fairly high temperature of over 300°C at around 2 km. Acoculco is the EGS site of the GEMex project with a high potential to be developed in the future.

The work presented in this report is investigating the thermal state of the subsurface at regional scale and associated resources available. To do so, the work has been performed by two teams, Utrecht University was responsible for the investigation of Los Humeros and CNR for Acoculco. The regional understanding of the considered sites is of great importance as it (1) provides boundary conditions for the more local thermal investigation of WP 6 and (2) allows to understand the processes and properties that define these two geothermal regions. Both teams used numerical models to study the emplacement conditions of the main heat source and used the same volumetric method to estimate the heat-in-place. The distinct geological and hydrothermal conditions as well as the data availability for the two fields, has led to two different modelling strategies being applied. The outcome of the thermal structure in the two sites is based first of all on a detailed geological understanding provided by both the European and Mexican team in WP4 and the geological modelling work of the BRGM and CNR in Task 3.1 (WP3) under a join EU-Mexico collaborative workflow. WP6 have provided petrophysical information making the model more accurate and the Mexican Hydrogeological team have provided vital information to understand the regional flow.

As a result of this work, we provide two state-of-the-art of the regional (hydro)thermal models based on all parameters concerning the heat source and fluid transport in both Acoculco and Los Humeros.

1 Introduction

Los Humeros and Acoculco are both large volcanic complex with a long lasting history including one or several. Both situated at the far east end of the Trans-Mexican Volcanic Belt, about 200 km north-west of Mexico City. Both sites have developed on a crystalline basement overlain by Cretaceous and Jurassic Limestone.

1.1 Los Humeros geological framework

Los Humeros volcanic complex (LHVC) is an active volcanic system (Fig. 1) with an active geothermal system located at the eastern end of the Trans-Mexican Volcanic Belt (TMVB), a volcanic arc that runs east-west as a result of the subduction of the Rivera and Cocos oceanic plates under the North American plate. The LHVC is the most northern volcano of the Serdán-Oriental Basin (SOB). LHVC is a Pleistocene basalt-andesite-rhyolite caldera that has developed on top of a crystalline basement of and a marine Cretaceous limestones (Carrasco-Núñez et al., 2017).

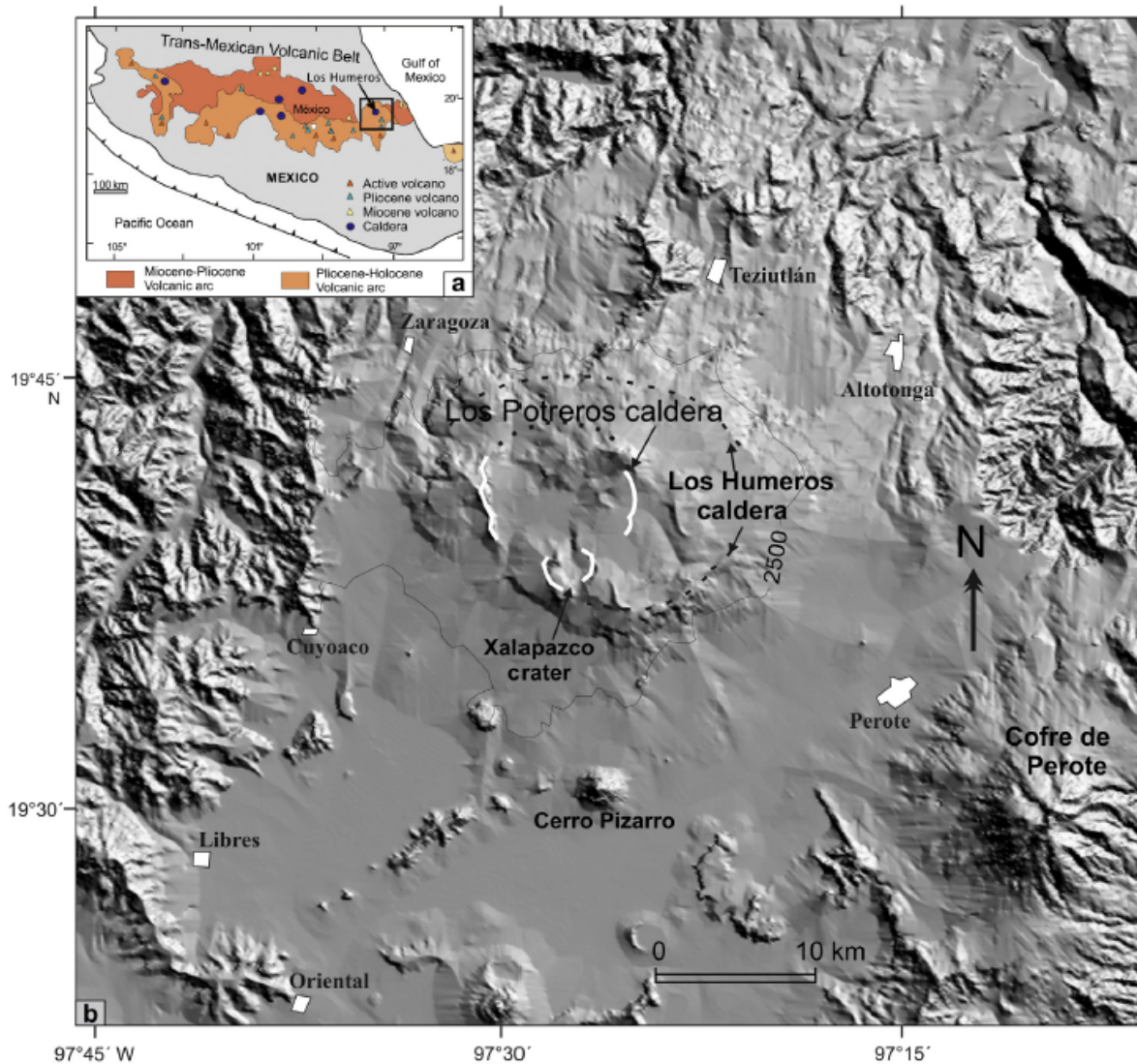


Figure 1: Location of Los Humeros caldera and geothermal field. a) Inset map showing the distribution in the eastern Trans Mexican Volcanic Belt (TMVB). b) Digital Elevation Model for Los Humeros showing the main structural features (Los Potreros and Los Humeros scarps) – from Carrasco-Núñez et al. (2017)

According to the most recent analysis of Carrasco-Núñez et al. (2018), the current volcanological formation, the caldera, has been formed in three stages. The first stage (pre-caldera) was of rhyolitic composition and place between 683.0 ± 1.7 ky and to 270 ± 15 ky. Following this ~ 400 kyr activity, the second stage created the main caldera of Los Humeros of 21 by 15 kms at 164 ky and is associated with the emplacement of a large ignimbrite due to a large explosive eruption. At the third stage (post-caldera stage), started 50 ky ago and and 4 ky. Within these 50kyr of post-caldera evolution, the compositions have changed from rhyodacitic and dacitic tuffs to basaltic andesitic and basaltic olivine-bearing lavas, reflecting an heterogeneous magmatic source.

Group	Unit	Rock	Age (Ma)
G1 Post-caldera	U1 Undefined pyroclastic	Tuff, pumice and some alluvium	< 0.003
	U2 Post-caldera	Rhyodacite, andesite, basaltic andesite, and olivine basalt lava flows	0.050 to 0.003
G2 Caldera	U3 Los Potreros caldera	Rhyodacitic flows Zaragoza ignimbrite	0.069
	U4 Intermediate caldera	Faby tuff with andesitic-dacitic lava flows	0.07
		Rhyolitic and obsidian domes	0.074
U5 Los Humeros caldera	Mainly composed of Xaltipan ignimbrite with minor andesitic and rhyolitic lava	0.165	
G3 Pre-caldera	U6 Upper pre-caldera	Rhyolite, dacite, some andesite and tuff, and minor basalt	0.693 to 0.155
	U7 Intermediate pre-caldera	Mainly pyroxene andesite (Teziutlán andesite) with mafic andesite in the basal part and/or dacite	2.61 to 1.46
		U8 Basal pre-caldera	Mainly hornblende andesite (Alseseca andesite and Cerro Grande) and subordinate dacite
G4 Basement	U9 Basement	Middle Miocene granite	15.12
		Cretacic limestone, shale and minor flint	~ 140
		Jurassic limestone and shale	~ 190
		Paleozoic granite and schist (Teziutlán Massif)	> 251

Table 1.1: Description of the geological formations in Los Humeros gathered into four groups and nine units (Calcagno et al., 2018)

The resulting sequence of deposition in the LHVC (Table 1.1) has been described by Calcagno et al. (2018), with three main groups that have ben identified: Pre-Caldera, Caldera, Post-Caldera. Based on their composition these groups have been further subdivided in eight units. In addition to these volcanic units and groups a basement layer has been describe that encapsulate the Palaeozoic granites and schists as well as the Jurassic and Cretaceous limestone

phenocrysts of olivine and plagioclase, and dacitic domes. The age of the ATVF spans from at least 2.25 ± 0.04 Ma to the Holocene (Avellán et al., 2018) (for an overview of the geological map of Acoculco see the map in Avellán et al., 2018).

The Acoculco caldera rocks in the area are deformed by three main fault systems: the NE-striking Tenochtitlán-Apan fault system, and the NW-striking Tulancingo-Tlaxco fault system. Locally, the Tenochtitlán-Apan fault system is represented by the Apan-Tlaloc and Chignahuapan faults, and the Tulancingo-Tlaxco fault system is represented by the Manzanito fault. The NE- and NW-striking normal fault systems intersect each other, creating an orthogonal arrangement of grabens, half-grabens and horsts (Sosa-Ceballos et al 2018).

The pervasive hydrothermal alteration in the central part of the Acoculco caldera has motivated considerable geothermal exploration. In the above mentioned exploration wells (i.e., EAC1 and EAC2) the temperature of 300°C at 2 km depth was measured, but no exploitable fluid has been discovered. Preliminary geological studies consider the site a candidate for the application of EGS technology to develop the field (Lorenzo-Pulido et al., 2010; Canet et al., 2015a). According to these studies, the geothermal target is probably located in the basement composed of calcareous, granitic and metamorphic rocks, since the overlying volcanic rocks show intense hydrothermal alteration (Calcagno et al., 2018).

2 Regional temperature structure of Los Humeros

2.1 Data

2.1.1 Temperature

The temperature in Los Humeros is constrained by the location of the wells at the centre of the caldera. In total 65 deep wells have been drilled in Los Humeros to explore or exploit the geothermal system. The temperature information retrievable from these wells is of three types: (1) temperature log series made of measurements every 6 hours for the first 24 hours after the drilling of the wells, (2) temperature log measured after weeks or months after drilling, and (3) temperature log while the well flows. The example of well H-43 (Fig. 3) show the return to equilibrium on the to the left and 20 days recovery and dynamic measurements to the right. For both recover and dynamic the flow in the well is clearly identifiable on the temperature log making them untrustworthy to be used to characterise the temperature before drilling. The time series however can be used to define formation temperature.

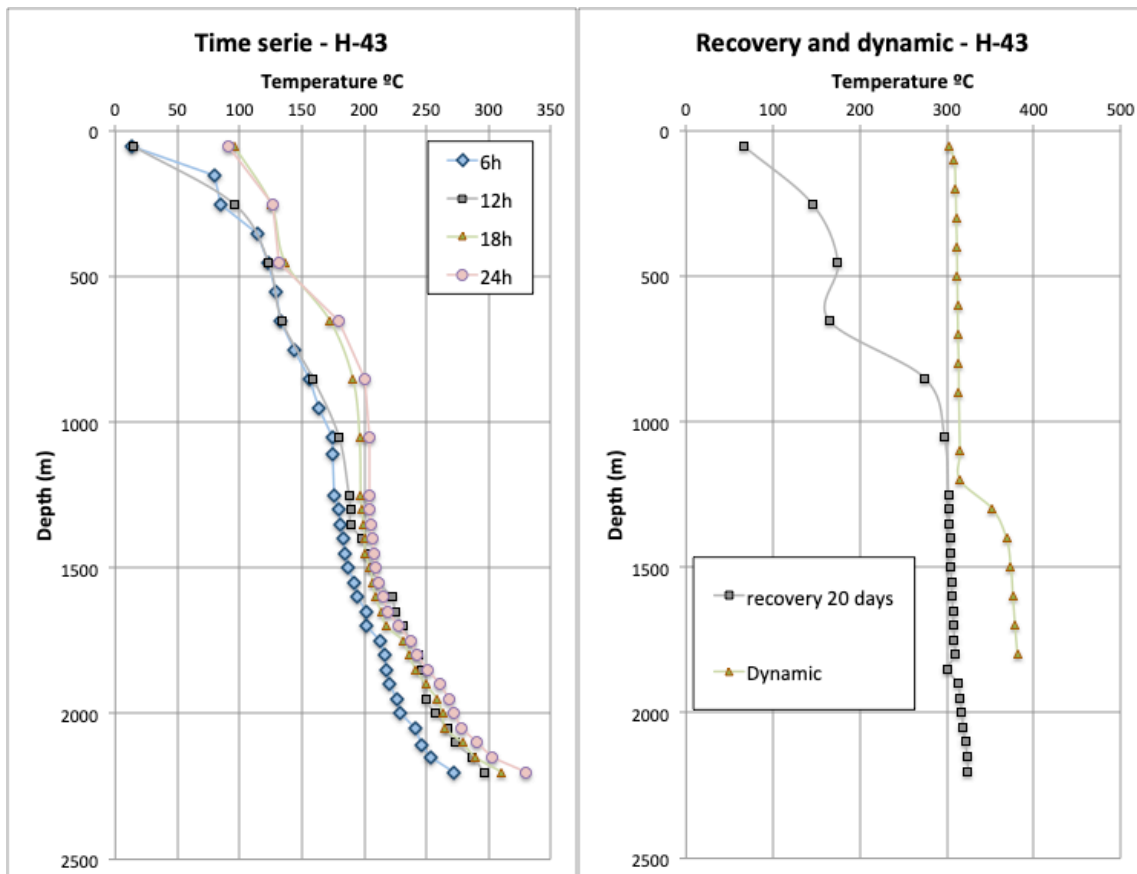


Figure 3: examples of temperature log in the well H-43. Left: time series within the day after drilling. Right: 20 days recovery and dynamic measurement.

The data from the time series in the wells has been kindly provided by the Comisión Federal de Electricidad (CFE). Within the 65 wells that have been drilled in Los Humeros, 52 were provided for investigation by the CFE leading to exploitable information in 49 wells. As some wells are deviated, a total of 54 temperature series are available (Fig. 4). However, to obtain a reliable value, a correction is necessary. The correction method is performed on the deeper measurement, the Bottom Hole Temperature (BHT). The principle is to

fit a regression curve to the time series BHT. We are using the Instant Cylinder Source (ICS) method from Goutorbe et al. (2007) allowing to obtain a close to equilibrium temperature.

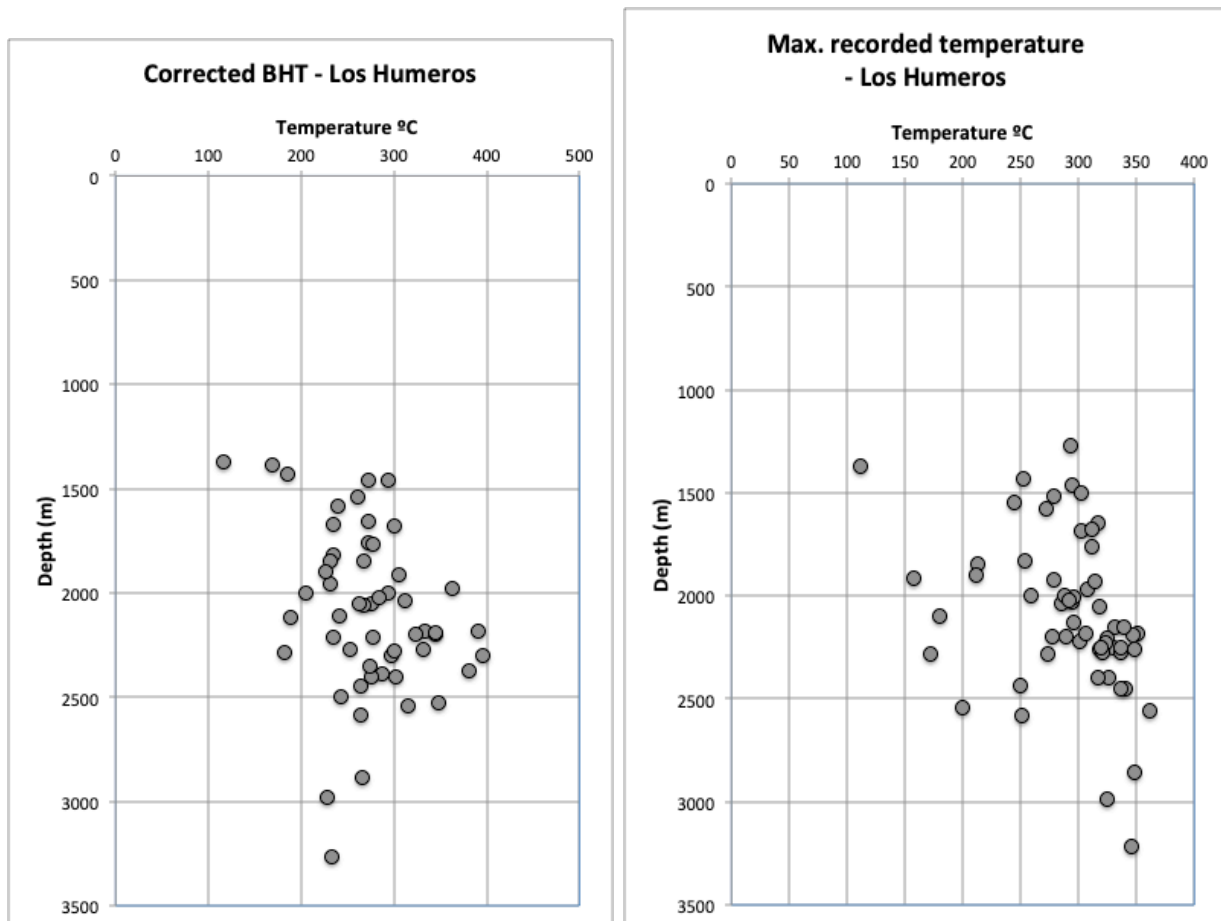


Figure 4: BHT temperatures in Los Humeros. Left: Time series BHT corrected using the ICS method. Right: Higher (and therefore deeper) temperature recoded on the logs with few weeks recovery.

The result obtained from these data is a cloud of reliable temperatures (Fig 4. left) between just over 100°C and nearly 400°C, for an average temperature in excess of 270°C. The temperatures are not homogeneously spread in the Los Humeros Caldera. By looking at the thermal gradient (Fig. 5), it is noticeable that the highest temperatures are in the northern part of the inner caldera and follow the main SW-NE faults. It is also obvious that the temperatures are widely irregular and are not in clusters.

The data used in the thermal modelling of Los Humeros are detail below in Table 2.2. For the first step of the modelling (see Model A in section 2.3), only the 3 blue wells in Table 2.2 has been used as they have been considered as been in purely convective mode and therefore where of importance to support the characterisation of the magmatic contribution to the thermal structure. For the later stages, all wells have been used, excluding the 6 wells marked in red in Table 2.2 as their altitude was uncertain. In total, the contribution of 48 temperature value allowed to characterise the thermal structure in Los Humeros

2.1.2 Geological model

The scale use for the modelling is based on the model created by GEMex task 3.1 and led by the BRGM. The geological model used is the regional model from Calcagno et al. (2018). The starting point to develop this model is the map published by Carrasco-Núñez et al. (2017), this map also defines the lateral extension of the model. In addition to the valuable initial information from the authors of Carrasco-Núñez et al. (2017), the work of Norini et al. (2015) has provided further constrains and knowledge. The contribution of the well information from CFE (Comision Federal de Electricidad) has also been significant in defining the volcanoclastic sequence in depth. Figure 7 show the geological model used for the thermal modelling of Los Humeros.

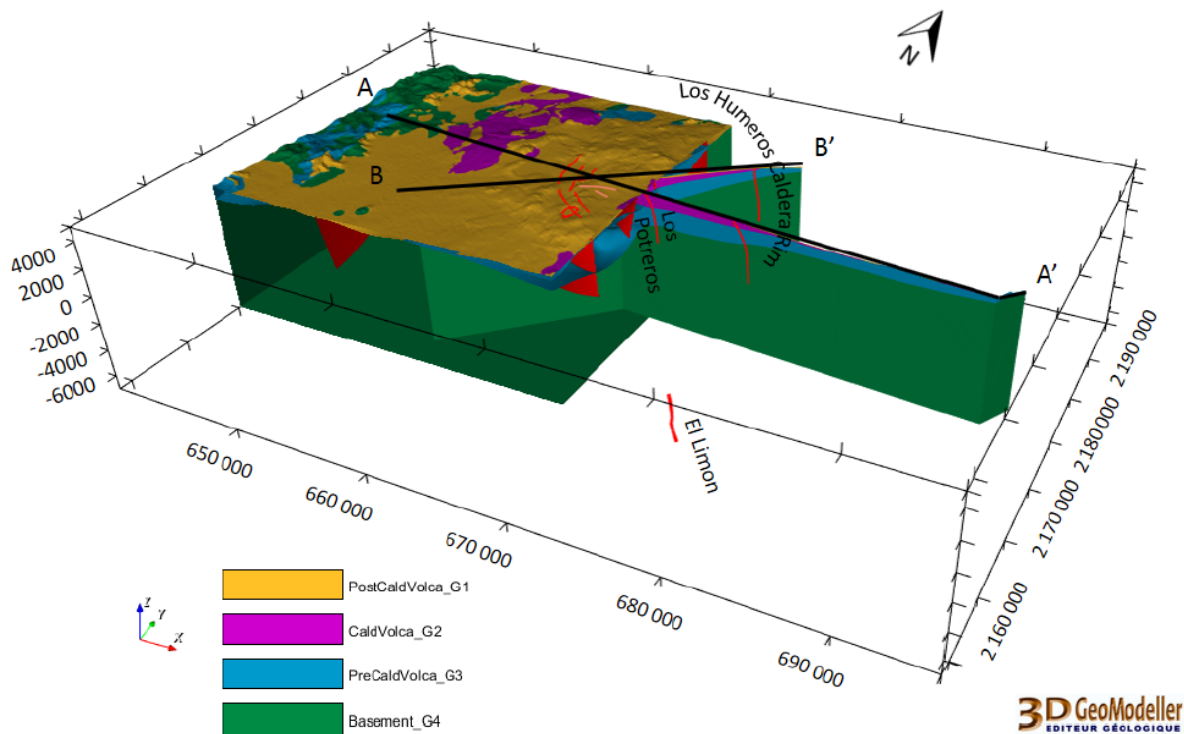


Figure 6: Humeros regional geological model including the fault model (see 3DLHRegionalFaultModel) and the four geological groups listed at bottom left. AA': Carrasco-Núñez et al. (2017a) cross-section, BB': Norini et al. (2015) cross-section. Source Calcagno et al., 2018.

The model consists of 128 by 128 by 52 cells (851968) and has a physical size of 56000 m x 36000 m x 20000 m in x,y,z . The top of the model is located at 5000 m above sea level (-5000 m) and extends to 15000 m below sea level (15000 m). The model has a horizontal resolution of 437.5 m for x and 281.25 m for y . The vertical resolution of the model changes with depth: for a depth z of 1000 meter below sea level, the cell size is 250 m and at deeper levels, it is 500 m. The layers are. The model consists of five main layers (Table 1) based on the preliminary geological model of Evanno (2017) and Calcagno et al. (2018). The first three layers (1-3) correspond directly to the groups G1-G3 (Table 1.1), while layer 4 corresponds to the top formations from the G4 group and layer 5 to the bottom formation granitic crustal basement G4.

2.1.3 Hydrogeology

Los Humeros Volcanic Complex (LHVC) is at the northern end of the Serdán-Oriental Basin (SOB), as such it is surrounded by height to the south-west (Cofre de Perote) and north-east (exhumed system between Aocolulco and Los Humeros). The feed of the Los Humeros geothermal system is mostly carried by the Cretaceous and Jurassic limestone that are below the volcanic deposit sequences. The heights surrounding the LHVC, where the limestone outcrop such as in the exhumed system to the northwest or where is it shallow below highly permeable volcanoclastic sediment such as near Cofre de Perote to the south east. In addition, the Basin is tilted to the north-east, creating the main flow direction in the limestone.

According to the work of T. Kretzschmar (pers. communication), the total watershed (Fig. 7) extend that recharges the system covers an area of 10227 km², which is more that the extend of the modelled area (2035 km²), and is composed of 6 individual watersheds. The total volume of water collected in these watersheds is 10.2 10⁹ m³ but the recharge of the Los Humeros geothermal system is only 2% (204.5 10⁶ m³)

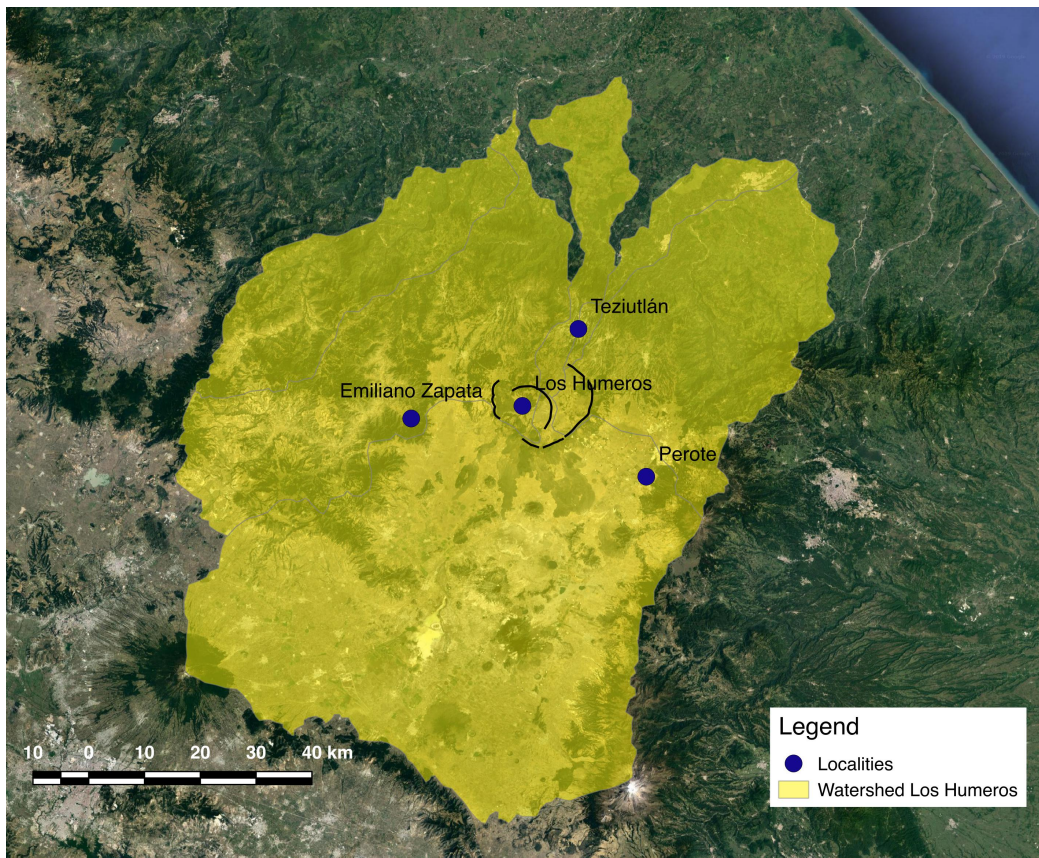


Figure 7: Los Humeros watershed (source: T. Kretzschmar)

The implication for the model is that all the recharge for the modelling is being made through the border via the limestone (blue polygon on Fig. 8). The reason for not having the recharge on the complete tour is due to the tilt of the limestone toward the northeast. However, the caldera is the outflow and the variability on the flow will be part of the adjustment made through the model iteration.

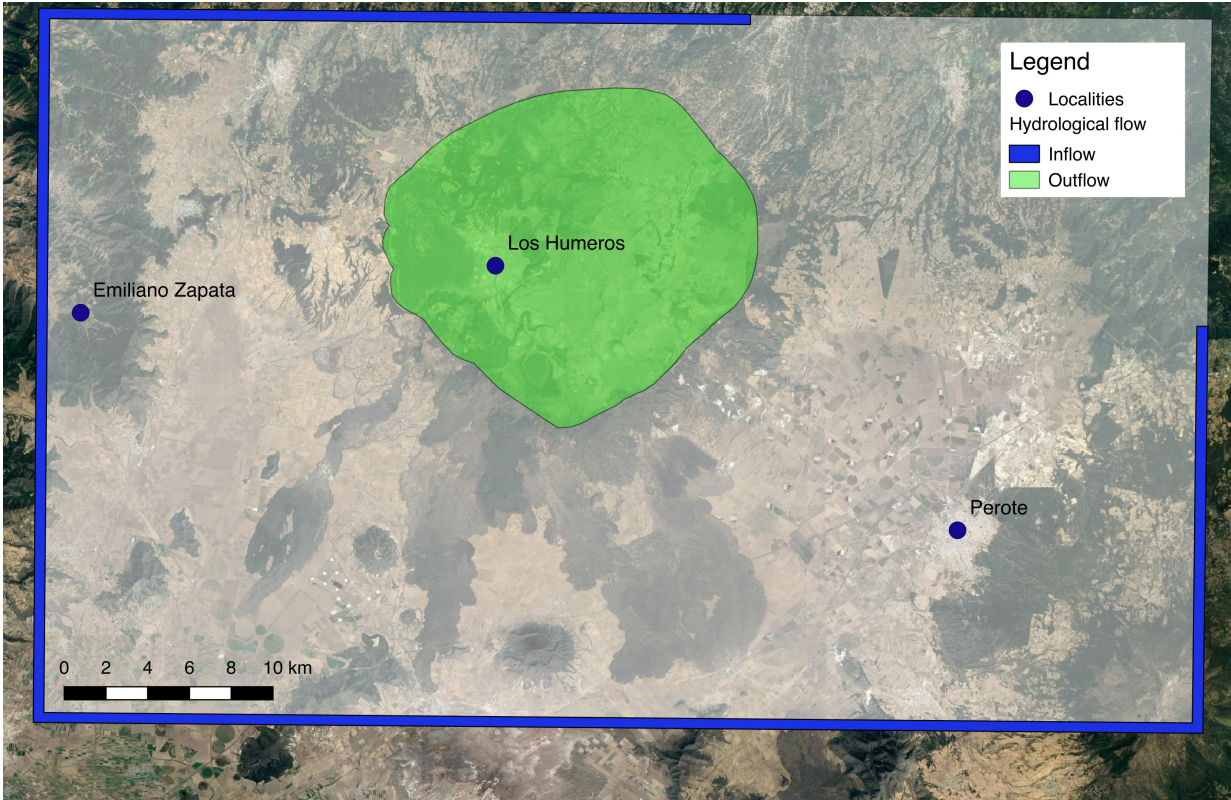


Figure 8: Inflow and Outflow for the Los Humeros

2.2 Methodology

The backbone of the methods used for calculating the thermal state of the Los Humeros area are based on an extension of the work of Limberger et al. (2018). In this work, the thermal state of the lithosphere is estimated, assuming steady-state conditions and conductive heat transfer only. For the Los Humeros model, the thermal field was initially calculated with a multi-1D, steady-state conductive thermal model to initialize temperature- and pressure-dependent thermal properties, before calculating the 3D steady-state conductive forward thermal model. This 3D steady-state conductive forward model is used as a reference model and serves as a base for superposition of (a combination of) non-steady-state and/or advective effects.

For all the models, 25°C and 600°C were assumed for the upper and lower boundary conditions after Verma & Gómez-Arias (2013; 2014). To study the effect of non-steady-state and/or advective effects, we used inverse modelling (see Section 2.2.5) on a selection of temperature measurements to find a suitable range for the magma chamber emplacement depth, regional groundwater fluxes, and local advection (see Section 2.3).

2.2.1 Model geometry and thermal properties

Each of the layers in the model consists of a single lithology or of a mixture of lithologies (Table 2.2 and 2.3). Bulk thermal conductivity for each layer is iteratively calculated, taking into account compaction effects and temperature/pressure dependence. Bulk radiogenic heat production is a fixed number for the matrix of each lithology (Table 2.3).

For the matrix thermal conductivity k_m of the different lithologies (Table 2.3), the empirically derived equation of Sekiguchi (1984) was used:

$$k_m = 358(1.0227 \lambda_i^{20} - 1.882) \left(\frac{1}{T} - 0.00068 \right) + 1.84 \quad (\text{Eq. 2.1})$$

where T is temperature in K, λ_i^{20} is the matrix thermal conductivity at room temperature, i denotes vertical or horizontal. The matrix conductivity is determined from rock samples, correcting the measured bulk thermal conductivity for porosity. Commonly, a geometric mixing law (Eq. 2.2) is assumed for the respective contributions of the solid and fluid parts of a rock to bulk thermal conductivity (Hantschel and Kauerauf, 2009):

$$k = k_m^{1-\phi} k_w^\phi \quad (\text{Eq. 2.2})$$

Depending on the rock type, other mixing laws might be more appropriate. k_w is thermal conductivity of water, which is approximately $0.6 \text{ W m}^{-1} \text{ K}^{-1}$.

Layer	Group	Mixture
Layer 1	G1 Post-caldera volcanics (yellow)	25% Tuff 25% Rhyodacite 25% Basalt 25% Andesite
Layer 2	G2 Caldera volcanics (purple)	50% Ignimbrite 25% Rhyodacite 15% Andesite 10% Tuff
Layer 3	G3 Pre-caldera volcanics (light blue)	60% Andesite 30% Rhyodacite 5% Basalt 5% Tuff
Layer 4	G4 Pre-volcanic basement (blue)	100% Marble
Layer 5	G4 Crustal basement (green)	100% Granite

Table 2.2: Layer lithology.

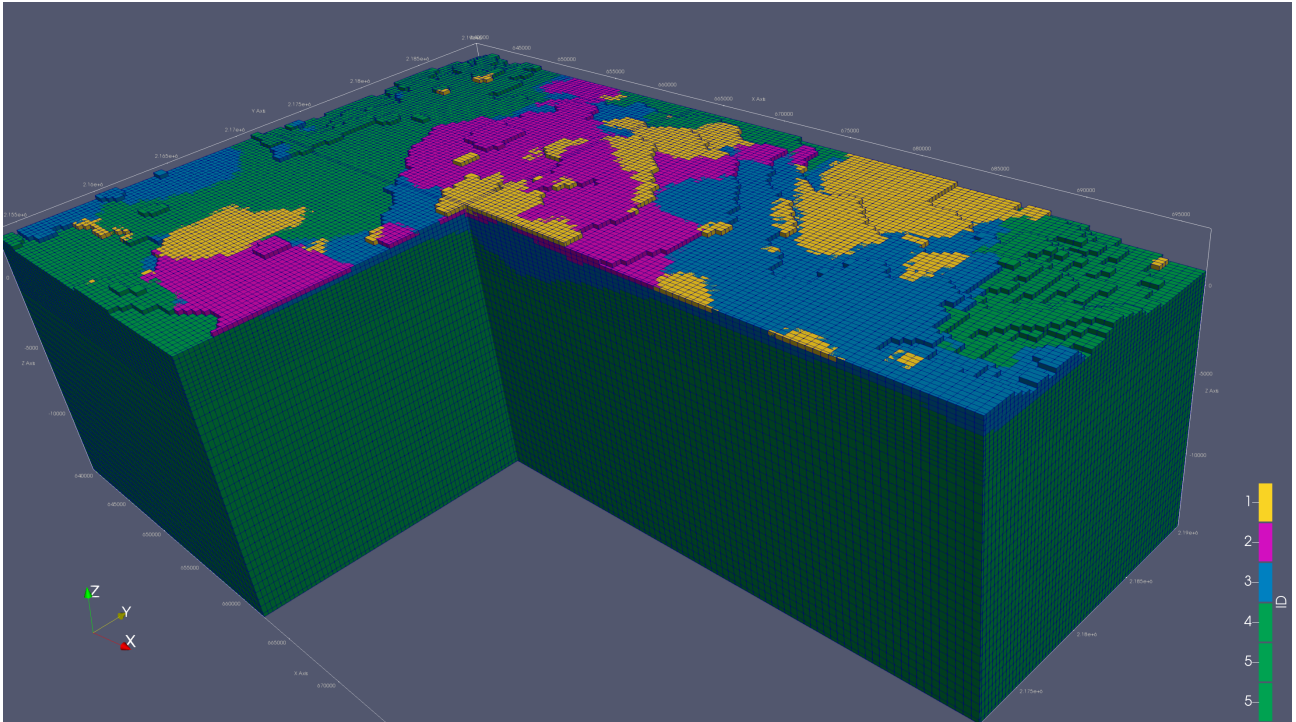


Figure 9: The parameterized model consisting of five main layers: three layers (1-3) correspond directly the groups G1-G3 (Table 1.1). Layer 4 corresponds to the top formations from the G4 group. Layer 5 corresponds to the bottom formation granitic crustal basement G4.

Lithology	K matrix [W/(mK)]	anisotropy	A [$\mu\text{W}/\text{m}^3$]	phi ₀ [%]
Granite	2.60	1.15	2.57	0.00
Andesite	1.74	1.00	0.64	13.45
Basalt	1.74	1.17	0.52	17.20
Ignimbrite	1.79	1.17	1.56	15.00
Marble	1.66	1.02	0.34	19.03
Rhyodacite	1.68	1.00	1.51	16.70
Tuff	1.99	1.17	1.56	12.43

*Except for granite all matrix thermal conductivity values are based on the dry values from the GEMex petrophysical database (Weydt et al., Task 6.1). The matrix thermal conductivity values of granite, along with other properties in bold font, are taken from the petrophysical database of Hantschel and Kauerauf (2009).

Table 2.3: Lithology and thermal properties.

2.2.2 Forward model

In an Eulerian² reference framework, the heat equation is:

$$\rho c_t \frac{\partial T}{\partial t} = \nabla \cdot (k_t \nabla T) + A - \vec{v} \nabla T \quad (\text{Eq. 2.3})$$

where T is temperature [K or C°], t is time [s], ρ is density [$\text{m}^3 \text{kg}^{-1}$], c_t is specific heat capacity [$\text{J kg}^{-1} \text{K}^{-1}$], k_t is thermal conductivity [$\text{W m}^{-1} \text{K}^{-1}$], A is radiogenic heat production [W m^{-3}], ∇ is the nabla operator: $\left(\frac{\partial}{\partial x}, \frac{\partial}{\partial y}, \frac{\partial}{\partial z}\right)^T$, \cdot is dot product, \vec{v} is the advective velocity, which can be the velocity of rock relative to a reference itself due to active tectonic deformation (e.g. Van Wees et al., 2009).

The advective velocity can also be a result of fluid flow inside pores or fractures, which can strongly affect the thermal distribution (e.g. Guillou-Frottier et al., 2013; Cherrubini et al., 2014). In absence of gravitational effect, the fluid velocity is resolved from solving the Darcy flow equation:

$$c_h \frac{\partial P}{\partial t} = \nabla \cdot \left(\frac{k_f}{\mu_f} (\nabla P) \right) + Q \quad (\text{Eq. 2.4})$$

where P is pressure [Pa], c_h is the bulk hydraulic storage capacity of the fluid [$\text{m}^3 \text{Pa}^{-1}$], k_f is bulk permeability [m^2], μ_f is fluid viscosity [Pa s], Q is source term [$\text{m}^3 \text{s}^{-1}$]. Through solving the pressure field P in (Eq. 2.4), the fluid velocities can be determined as:

$$\vec{v}_f = \frac{k_f}{\mu_f} (\nabla P) \quad (\text{Eq. 2.5})$$

And these can be incorporated in (Eq. 2.3) by adopting:

$$\vec{v} = \varphi \frac{\rho_f c_f}{\rho c_t} \vec{v}_f \quad (\text{Eq. 2.6})$$

where φ is rock porosity [dimensionless] and c_f is specific heat capacity [$\text{J kg}^{-1} \text{K}^{-1}$] of the fluid. In regional models, the heat equations (Eq. 2.3; Eq. 2.4) can be solved in a coupled manner to take into account the effects of fluid flow affecting the thermal structure. In most studies it is found that thermal perturbations due to fluid flow can be significant both (Beglinger et al., 2012; Guillou-Frottier et al., 2012; Cherrubini, 2014).

For the effect of fluid flow processes on timescales of 10s to millions of years, it is commonly assumed that Eq. 2.4 can be solved for a steady-state solution, so that the left-hand side is zero. At these timescales to construct a representative temperature model at crustal scale, Eq. 2.3 is typically solved in a steady-state mode (Cloetingh et al., 2010; Limberger and Van Wees, 2013; Scheck-Wenderoth et al., 2014). In doing so, it is assumed that incorporating the effects kinematic active deformation and fluid flow is not relevant on the large scales as the advective effects of \vec{v} related to sedimentation, erosion and/or fluid flow have no significant temperature effect. In most settings in Europe the velocities for sedimentation and erosion at the scale of a basin and crust up to 10 km depth are indeed not sufficient to cause a significant thermal perturbation deviating from a steady-state approximation and therefore justify a conductive approach for constructing a large-scale thermal model (cf. Cloetingh et al., 2010). This assumption is also justified by a good fit between temperatures predicted by steady-state conductive simulations and observed temperatures (Scheck-Wenderoth et al., 2014). We also adopt this approach for the initial temperature distribution of the

² In an Eulerian model representation, the model discretization is fixed and mass and fluids move through the model.

crust underlying Los Humeros and Acoculco. These thermal fields have been influenced by magmatism and fluid which have to be superposed on the steady state model.

2.2.3 Magmatism

Starting from a steady state model for the lithosphere, the effect of magmatism is incorporated by emplacing a magma body at an emplacement time, which instantaneously modifies the temperature of the eulerian grid. Subsequently for the remainder of the time the transient heat equation is numerically solved deploying a Runge-Kutta method (Van Wees et al., 2009). The Latent heat of the magma chamber is incorporated. This can be done incorporating a temperature dependent heat capacity or by adopting a correction for the emplacement temperature of 200 °C in agreement with the latent heat energy released during cooling (Spear, 1993; Paterson et al., 1998). Close to the magma chamber the latter results in an exaggeration of the predicted temperatures during cooling. However further away, in the depth range of temperature observations this has no effect. The geometry of the magma body is represented by an oblate spheroid, with the short axis vertical and the symmetry around the vertical axis. In the modelling a key uncertainty is the size as well as the depth of the magma chamber. These parameters strongly control the spatial extent and the geothermal gradient of the thermal anomaly observed in the Acoculco and Los Humeros geothermal reservoirs. Therefore, the thermal models presented below allow to constrain these parameters both for Acoculco and Los Humeros through finding best fit of model predictions to the temperature observations.

2.2.4 Hydrothermal fluxes

Superposed on the magmatic transient effects after its emplacement time, the hydrothermal fluid flow can strongly affect the thermal field. In the Los Humeros field, we have investigated the potential effect of the hydrothermal flow, by adopting a very simple hydrogeological model. Its prime aim has been to show the strong influence of deep-water circulation on the thermal field. The hydrothermal flow field is calculated in the 3D model with the following boundary conditions and flow properties:

- A deep (carbonate) flow zone is assumed (in blue, Fig. 10), represented by a permeable layer in the eulerian 3D grid corresponding to cells with k -index in the range $k_{top} < k < k_{base}$.
- The surface influx and outflux feeding to the deep flow zone is represented through a single input grid with $Q(x,y) > 0$ and $Q(x,y) < 0$ corresponding to the hydrological recharge (q_r) or discharge value (q_d) respectively. The sum of these fluxes is zero.
- The Q -values are chosen such that they represent flux values which are thought to be connected to the deep flow circulation in the carbonates. At x,y location where influx or outflux is present, the permeable layer is therefore overlain by a vertical flow conduit marked by a very high vertical and horizontal permeability (K_v/K_h) ratio.
- The flow field is solved using eq. 2.4 for steady state conditions using Q and the permeability field above, and assuming no flow in or out of the model, except for $Q(x,y)$ at surface.

The flow field can be varied in two ways in ensemble runs to fit model predictions to observations:

- Variation by a scaling factor of the input Q -grid by a constant factor (called natural flux scaling).
- Applying a shift (called shift) in the q_d -values marked by relatively short range variogram to allow for spatial variations in discharge resulting in spatial variations in the thermal gradient. The q_r -values are scaled by a constant factor to ensure mass conservation in the flow field.

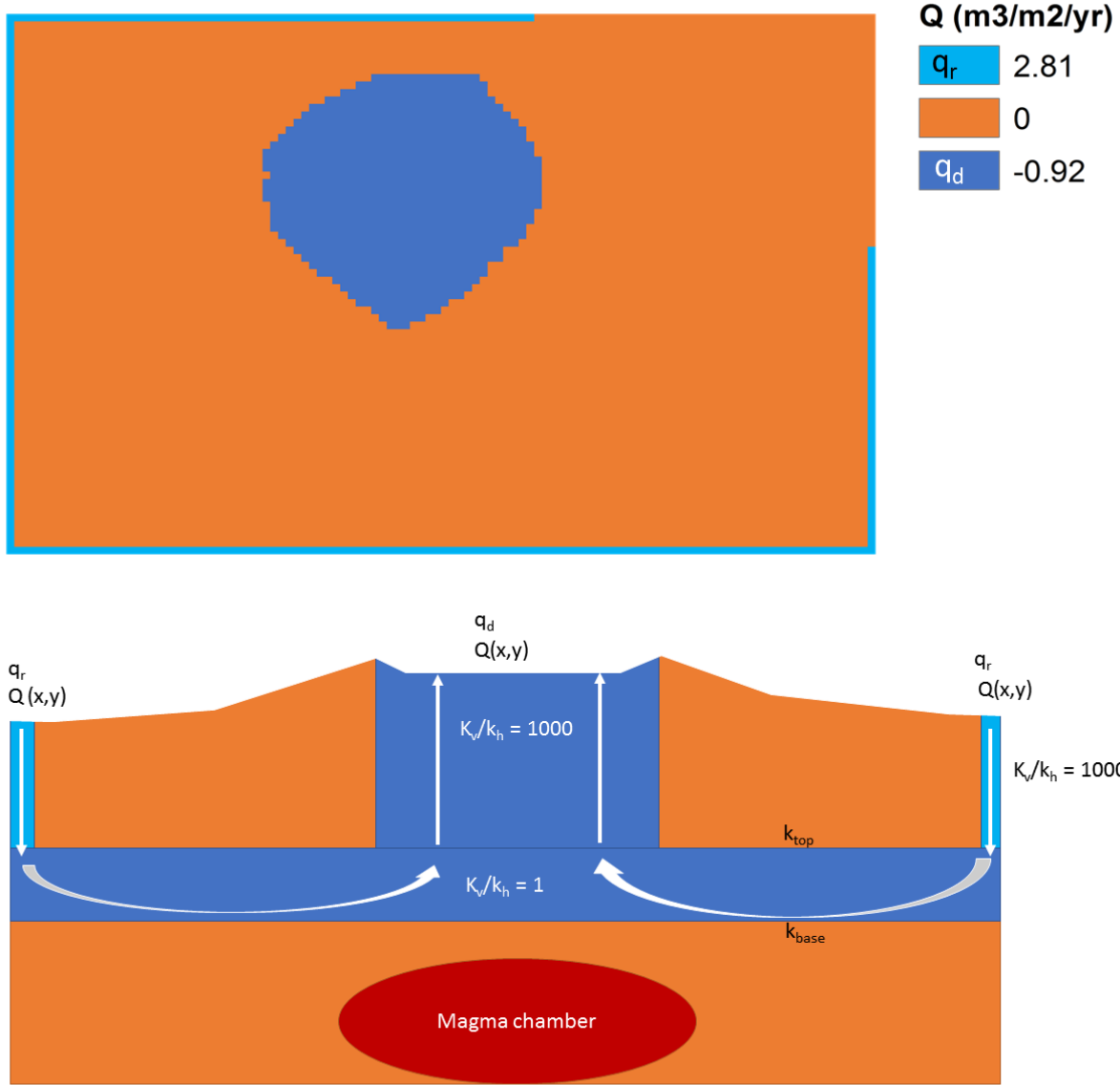


Figure 10: (top) Hydrothermal boundary conditions of recharge (at the sides of the model, q_r) and discharge (at the caldera q_d). (bottom) Schematic section of the recharge and discharge boundary conditions and the simplified hydrogeological model to calculate the 3D flow field (with Eq. 2.4). The resulting flow field is used as \vec{v} in (Eq. 2.3).

2.2.5 Data assimilation

The goal of this inversion is to obtain information about the thermal state of our model from the set of observations. For each data assimilation sequence, multiple iterations N_a were performed using an inflated covariance matrix C_d of the observation errors. Each iteration returned an ensemble that was based on a predefined number of ensemble members runs N_e where one or more variables were varied with Monte Carlo Sampling, following the prior probability distributions and variograms of the model parameters.

\mathbf{m}	$n \times 1$	model vector
\mathbf{d}_{obs}	$m \times 1$	data vector
ϵ	$m \times 1$	data error vector
\mathbf{C}_m	$m \times m$	model covariance
\mathbf{C}_d	$n \times n$	data covariance
\mathbf{G}	$m \times n$	linear(ized) measurement operator matrix

$\mathcal{G}(\mathbf{m})$ $m \times l$ non-linear measurement operator (predicted value)

where n is the number of degrees of freedom in the model parameters, and m the number of observations. For most geophysical problems, n is much larger than m . With only 47 data points available and a total number of more than 800000 cells in this model, the inverse problem is ill-posed and model solutions are therefore non-unique. An optimization routine was used for this model to minimize the cost function of the form:

The goal of inversion is to minimize the cost function of the form:

$$J(\mathbf{m}^a) = (\mathcal{G}(\mathbf{m}^a) - \mathbf{d}_{obs})^T \mathbf{C}_d^{-1} (\mathcal{G}(\mathbf{m}^a) - \mathbf{d}_{obs}) + (\mathbf{m}^a - \mathbf{m})^T \mathbf{C}_m^{-1} (\mathbf{m}^a - \mathbf{m}) \quad (\text{eq. 2.7})$$

Where \mathbf{m}^a denotes the posterior (assimilated) model vector, based on prior model vector \mathbf{m} . Bold characters denote vectors and matrices when capitalized. The superscript T denotes the transposed value. Each model perturbation leads to variation away from the initial state of the model in order to fit the observations. The costs of each variation away from the initial state is dependent on the prior distribution of the parameters, and is balanced against the model misfits.

Ensemble smoother

In the ensemble smoother, the equation for the multiple data assimilation to minimize (Eq. 2.7) can be written as (e.g. Emerick and Reynolds, 2013):

$$\mathbf{m}^a_j = \mathbf{m}_j + \hat{\mathbf{C}}_{md} (\hat{\mathbf{C}}_{dd} + \mathbf{C}_d)^{-1} (\mathbf{d}_j - \hat{\mathbf{d}}_j) \quad (\text{Eq. 2.8})$$

For $j = 1, 2, [\dots], N_e$ with N_e denoting the number of ensemble members. Each ensemble consists of a stochastically sampled model parameter realization, and associated model forecast. So N_e model realizations are required for the number of ensembles N_a . $\hat{\mathbf{d}}_j = \mathcal{G}(\mathbf{m}_j)$ denotes forecasted values by the thermal model at the observation points. $\mathbf{d}_j = \mathbf{d}_{obs} + \boldsymbol{\epsilon}_j$, where $\boldsymbol{\epsilon}_j = \sqrt{\mathbf{C}_d} \mathbf{z}_j$, and $\mathbf{z}_j \approx \mathcal{N}(0, \mathbf{I}_{Nd})$. So \mathbf{z}_j are n uncorrelated samples of the normal distribution. The $\sqrt{\mathbf{C}_d}$ can be found from eigenvalues and eigenvalue analysis. Alternatively, $\boldsymbol{\epsilon}_j$ can be determined from adopting standard sequential Gaussian simulation methodologies adopting covariance matrix \mathbf{C}_d . The model parameters perturbations in the ensemble are determined in a similar way. So $\mathbf{m}_j = \mathbf{m} + \boldsymbol{\epsilon}_j$, where $\boldsymbol{\epsilon}_j = \sqrt{\mathbf{C}_m} \mathbf{z}_j$. $\hat{\mathbf{C}}_{md}$ and $\hat{\mathbf{C}}_{dd}$ are determined from the ensemble runs:

$$\hat{\mathbf{C}}_{md} = \frac{1}{N_e - 1} \mathbf{M}' \mathbf{D}'^T \quad (\text{Eq. 2.9})$$

$$\hat{\mathbf{C}}_{dd} = \frac{1}{N_e - 1} \mathbf{D}' \mathbf{D}'^T \quad (\text{Eq. 2.10})$$

Which are covariance matrix estimates, with $\mathbf{M} = \{\mathbf{m}_0, \mathbf{m}_1, [\dots], \mathbf{m}_{N_e}\}$, $\mathbf{D} = \{\mathcal{G}(\mathbf{m}_0), \mathcal{G}(\mathbf{m}_1), [\dots], \mathcal{G}(\mathbf{m}_{N_e})\}$, and primes denote column vectors consisting of anomalies with respect to the mean value of that particular column.

The ensemble smoother of Eq. 2.8 gives a direct solution if a linear relationship exists between model parameters and forecast. If that is not the case, such as for radiogenic heat production and thermal conductivity, the ensemble smoother needs multiple iterations.

Emerick and Reynolds (2013) introduced a procedure to improve the data matches obtained with an Ensemble Smoother (ES) for non-linear problems based on assimilating the same data multiple times with an inflated covariance matrix of the measurement errors (C_d). This procedure – denoted as ES-MDA – can be interpreted as an iterative ES, where the number of iterations N_a has to be chosen a priori. The ES-MDA method can be summarized as follows:

1. Define the number of iterations of the data assimilation N_a , and the multiplication coefficients of the data covariance matrix α_i , for $i = 1, 2, [\dots], N_a$;
2. Initialize the ensemble model parameters \mathbf{m}_j , using sequential gaussian simulation based on model prior estimate \mathbf{m} and parameter covariance matrix \mathbf{C}_m ;
3. For $i = 1$ to N_a :
 - a. Perturb the ensemble of observations, replacing \mathbf{C}_d with $\alpha_i \mathbf{C}_d \rightarrow \epsilon_j = \sqrt{\alpha_i} \sqrt{\mathbf{C}_d} \mathbf{z}_j$
 - b. Update the ensemble \mathbf{m}_j using eq. 2 with the scaled $\alpha_i \mathbf{C}_d$

2.3 Model results

The Los Humeros geothermal field has been in operation for several decades. The ~60 well have yielded important information on reservoir properties and the thermal state of the region. This has allowed estimates on emplacement depth, temperature, and the size of the magmatic heat source. Our numerical approach solves the transient heat and mass transport equations to estimate the present-day temperature distribution around a single magmatic heat source, associated with the ~0.164 Kya ignimbrite eruption (Carrasco-Nuñez et al. (2018)). Later magmatism, associated with post-caldera resurgence has not been taken into account.

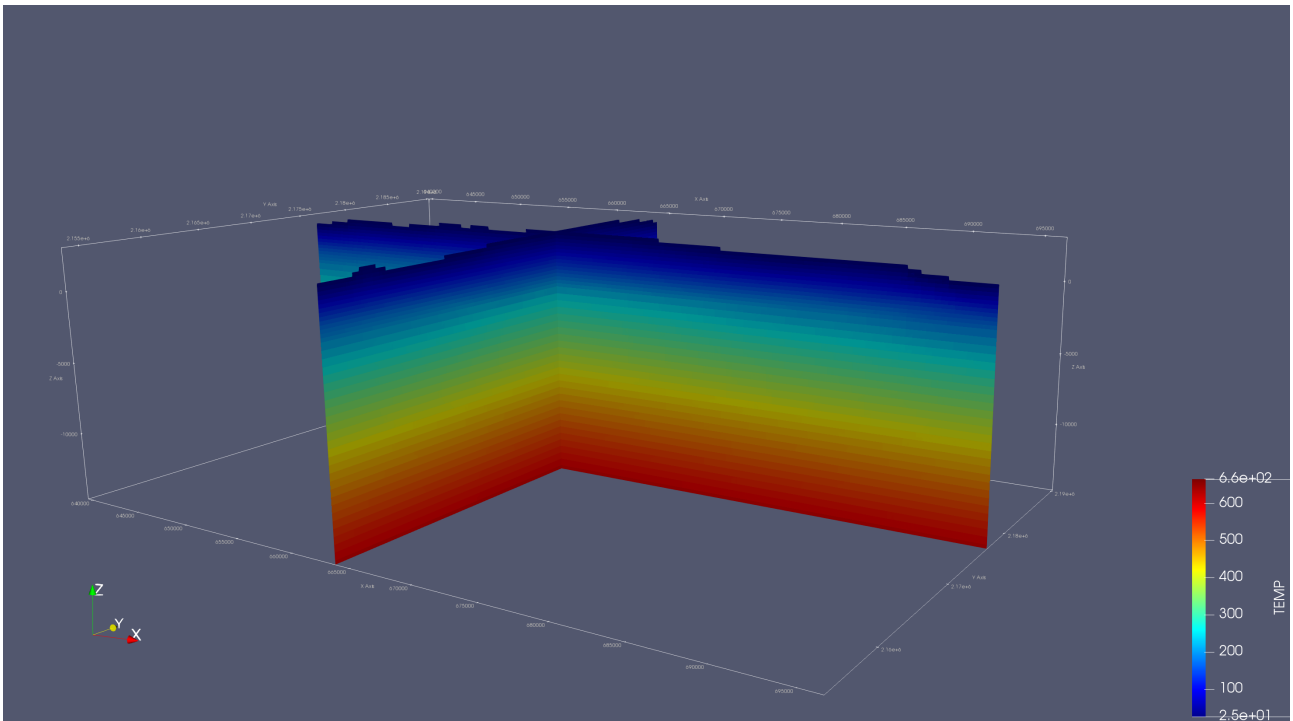


Figure 11: N-S and W-E cross sections through the steady-state conductive thermal field.

	A	B	C	D	E
Parameter	Z magma	Z magma	Q	q _d	q _d
Variation (shift/scale)	scale	scale	scale	shift	shift
Shift/Scale factor	0.1z, z, 1.5z	0.1z, z, 1.5z	0.1z, z, 1.5z	0.1q _d ±5	0.5q _d ±2.5
Distribution	Triangular	Triangular	Triangular	Uniform	Uniform
Variogram range	Global effect	Global effect	Global effect	2 cells	2 cells
Thickness hydro-layer	n/a	n/a	1 km	5 km	1 km
Magma chamber z	5 km	5 km	5 km	5 km	2.5 km
Temperature data	H5, H14, H25	All wells	All wells	All wells	All wells

Table 2.4: Parameter variation for the different models. All models were run with 4 iterations ($N_a = 4$) with 200 model realizations ($N_e = 200$).

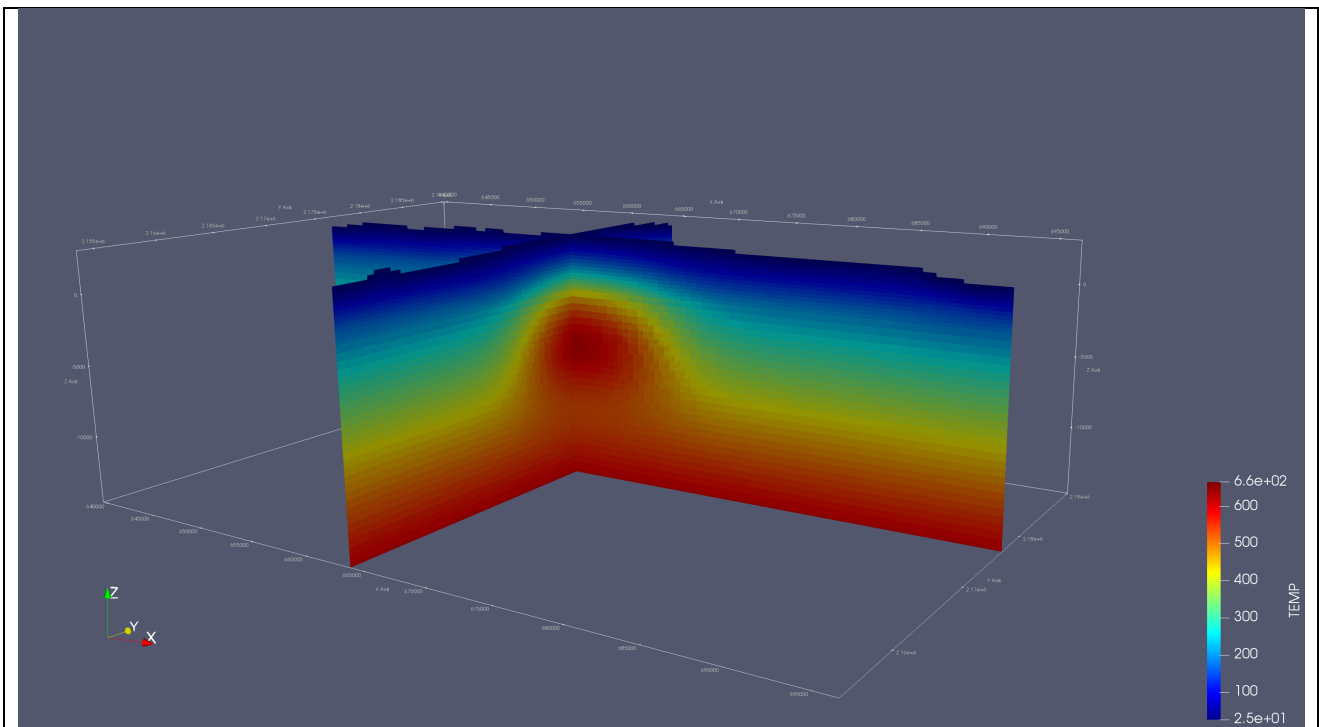
2.3.1 Magmatism results

A starting age for the cooling of 164 Kya was assumed, with an initial temperature of the magma body of 950 °C, following the new ages from Carrasco-Nuñez et al. (2018). Because the model does not yet include the effect of latent heat of crystallization, 200°C was added to the initial emplacement temperature (Spear, 1993; Paterson et al., 1998). The centre of the magma body was set at the centre of the caldera, at a default depth of 5 km below sea level (Giordano et al., Task 3.1). For the magma radius, 9500 m was assumed in the *xy*-direction and 1500 m for the *z*-direction, resulting in a magma volume of $\sim 1134 \text{ km}^3$. This magma volume is in in range with the most conservative estimate of Carrasco-Nuñez et al. (2018).

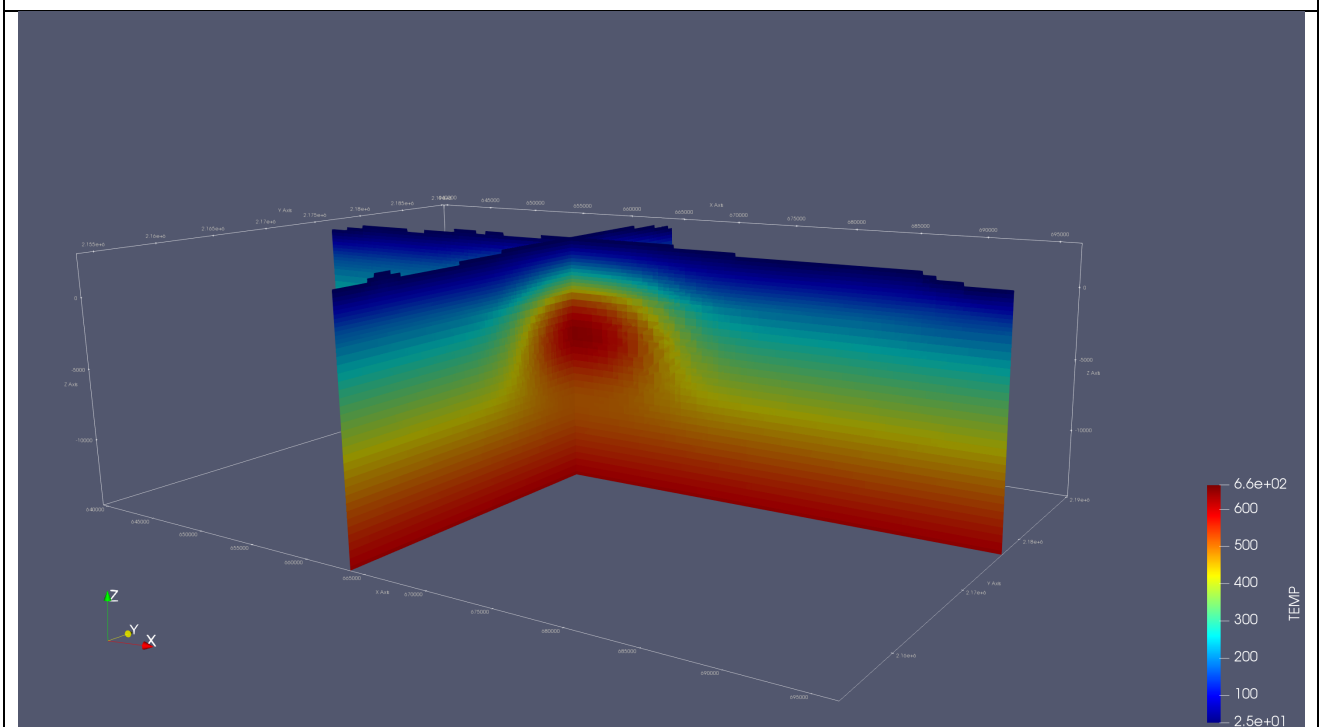
The magma chamber emplacement depth was varied for two models with a scaling factor randomly sampled from a triangular distribution, allowing variation between 0.1 and 1.5 times the default emplacement depth of 5 km below sea level.

For the first model, only temperature measurements were used from wells H5, H14, H25; likely showing a conductive thermal signal. A reasonable fit (Fig. 13a and 13c) was obtained with the three wells for a magma chamber emplacement depth of $\sim 4100 \pm 1000$ m below sea level (Fig. 12a). This value is in agreement to the initial estimate of 5000 m below sea level.

For the second model, all available temperature measurements were used (Section 2.1), resulting in a shallower magma chamber emplacement depth of 3275 ± 170 m below sea level (Fig. 12b). However, the resulting poor fit (Fig. 13b and 13d) with the complete well dataset suggests that the emplacement of a single magma chamber is likely not the only process that controlling the thermal field of the Los Humeros region.



a



b

Figure 12: N-S and W-E cross sections through the thermal model based on the mean calculated temperatures after stochastically varying the emplacement depth of the heat source. (a) For the top model (model A in Table 3), wells H5, H14, H25 were used for calibration. (b) For the bottom model (model B in Table 3), all available wells were used, resulting in a shallower heat source.

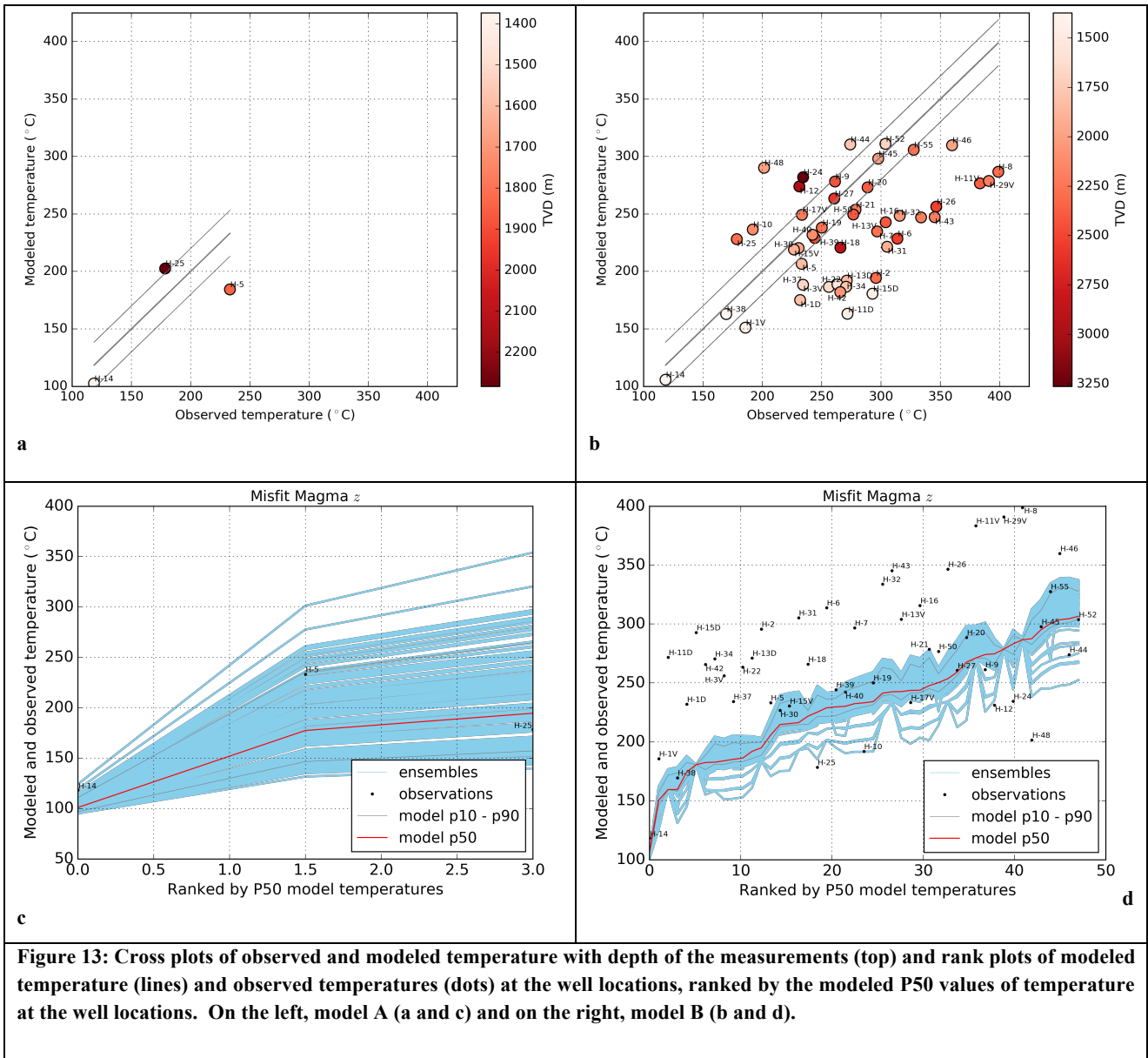


Figure 13: Cross plots of observed and modeled temperature with depth of the measurements (top) and rank plots of modeled temperature (lines) and observed temperatures (dots) at the well locations, ranked by the modeled P50 values of temperature at the well locations. On the left, model A (a and c) and on the right, model B (b and d).

2.3.2 Magmatism combined with regional groundwater fluxes

Following the results of the models with a magmatic heat source emplacement, it was decided to add the hydrothermal effects of deep-water circulation to obtain an improved fit with the observed temperatures. We tested three scenarios (Table 2.4). The same assumptions from Section 2.3.1 for the size, shape and timing of the magma emplacement were used. For model C, the regional effect of deep-water circulation and up-flow in the caldera-zone was combined with the emplacement of a magmatic heat source at 5 km below sea level. It was assumed that hydrothermal activity started 5 Kya. The hydrothermal flux Q was varied globally with a scaling factor randomly sampled from a triangular distribution, allowing variation between 0.1 and 1.5 times the original values.

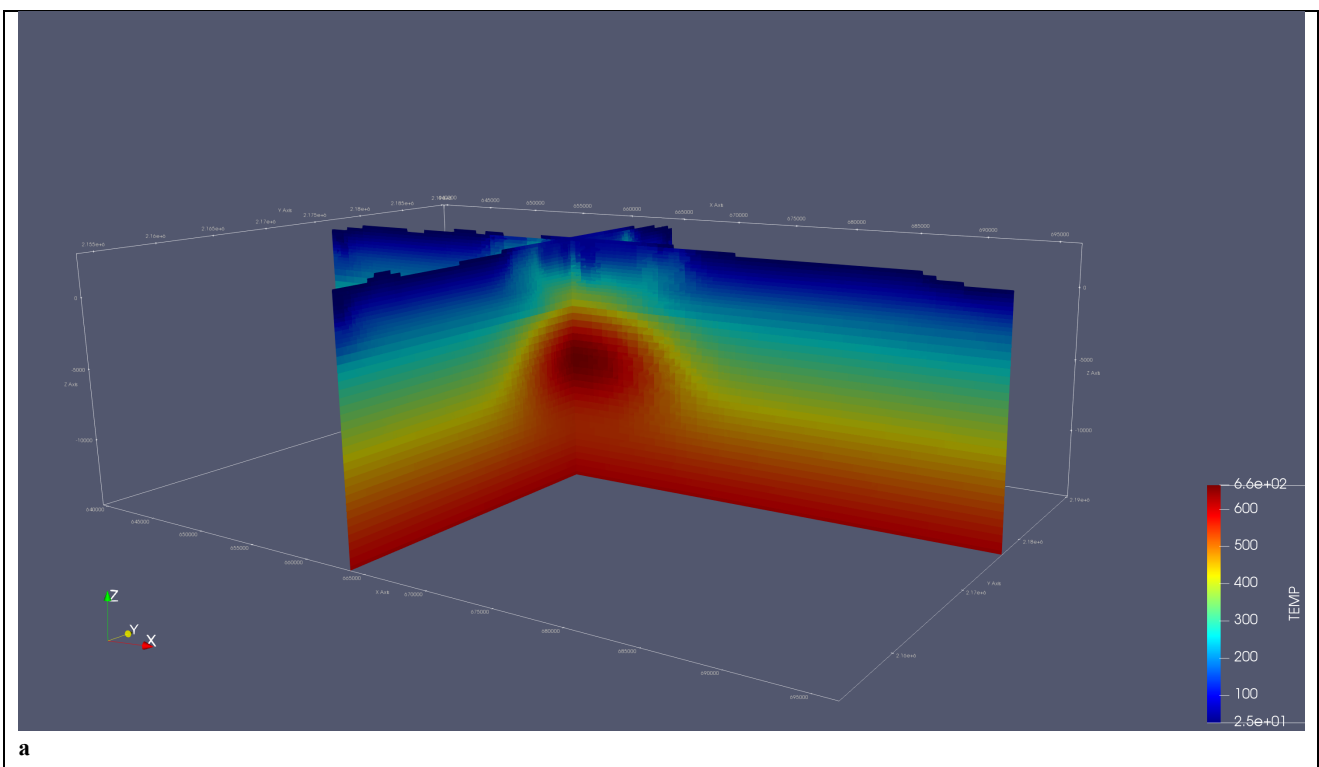
Model D combines the regional effect of deep-water circulation with spatial variation of flow (q_d and q_r) in the caldera zone, and the emplacement of a magmatic heat source at 5 km below sea level. The best fit was obtained by scaling the natural flux Q with 0.5, before shifting the local discharge q_d by a value randomly sampled from a uniform distribution between +5 and -5. The sum of the total q_d and q_r is kept at zero by

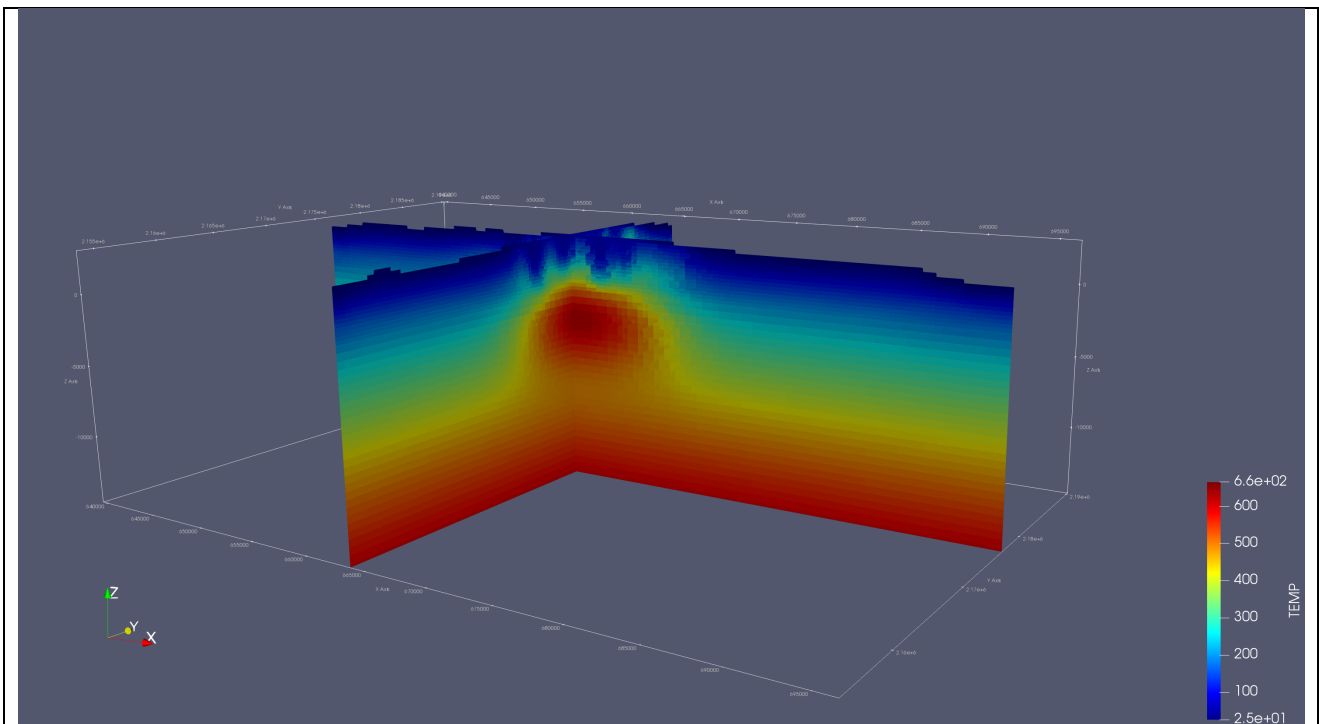
adjusting the q_r accordingly. To incorporate the effect of locally adjusted surface sources (q_d and q_r) into each thermal model run, the hydrological model was updated and the resulting fluxes used as input for the thermal model.

Model E differs from model D by a shallower magma emplacement of 2.5 km below sea level and scaling the a natural flux Q with 0.1, before shifting the local discharge q_d by a value randomly sampled from a uniform distribution between +2.5 and -2.5.

Both models show a reasonable fit with the wells used for the inversion (Fig. 15). The main difference is that model D underestimates the temperature for most of the misfit well (outside the predefined $\pm 20^\circ\text{C}$ error bandwidth (Fig. 15a)), while model E mostly overestimates temperatures for these misfit wells. What becomes clear from the misfit maps is that over- and underestimated values are in some cases very close-within one or two model cells-to each other. This could indicate that the model horizontal and vertical resolution might be a limiting factor for finding the best fit, as it limits the capability to simulate advective heat transfer via small-scale faults and fractures.

Other limiting factors are the single layer and vertical conduit, the input fluxes, the assumed ratio between precipitation and infiltration, and the onset of hydrothermal activity at 5 Kya. The evolution of the Los Humeros Volcanic Complex also consists of more phases than the single magmatic heat source emplacement assumed in these models (Giordano et al., Task 3.1; Carrasco-Nuñez et al. (2018)). Multiple heat sources, rejuvenation of existing heat sources, and bimodal volcanism could have a significant impact on the results.





b

Figure 14: N-S and W-E cross sections through the thermal model based on the mean calculated temperatures after stochastically varying the hydro fluxes. (a) For the top model (model D, Table 3), the emplacement depth of the heat source was set at 5 km below sea level, while the thickness of the hydraulically conductive layer was increased to 5 km. (b) For the bottom model, the emplacement depth of the heat source was set at 2.5 km below sea level, while the thickness of the hydraulically conductive layer was kept at 1 km.

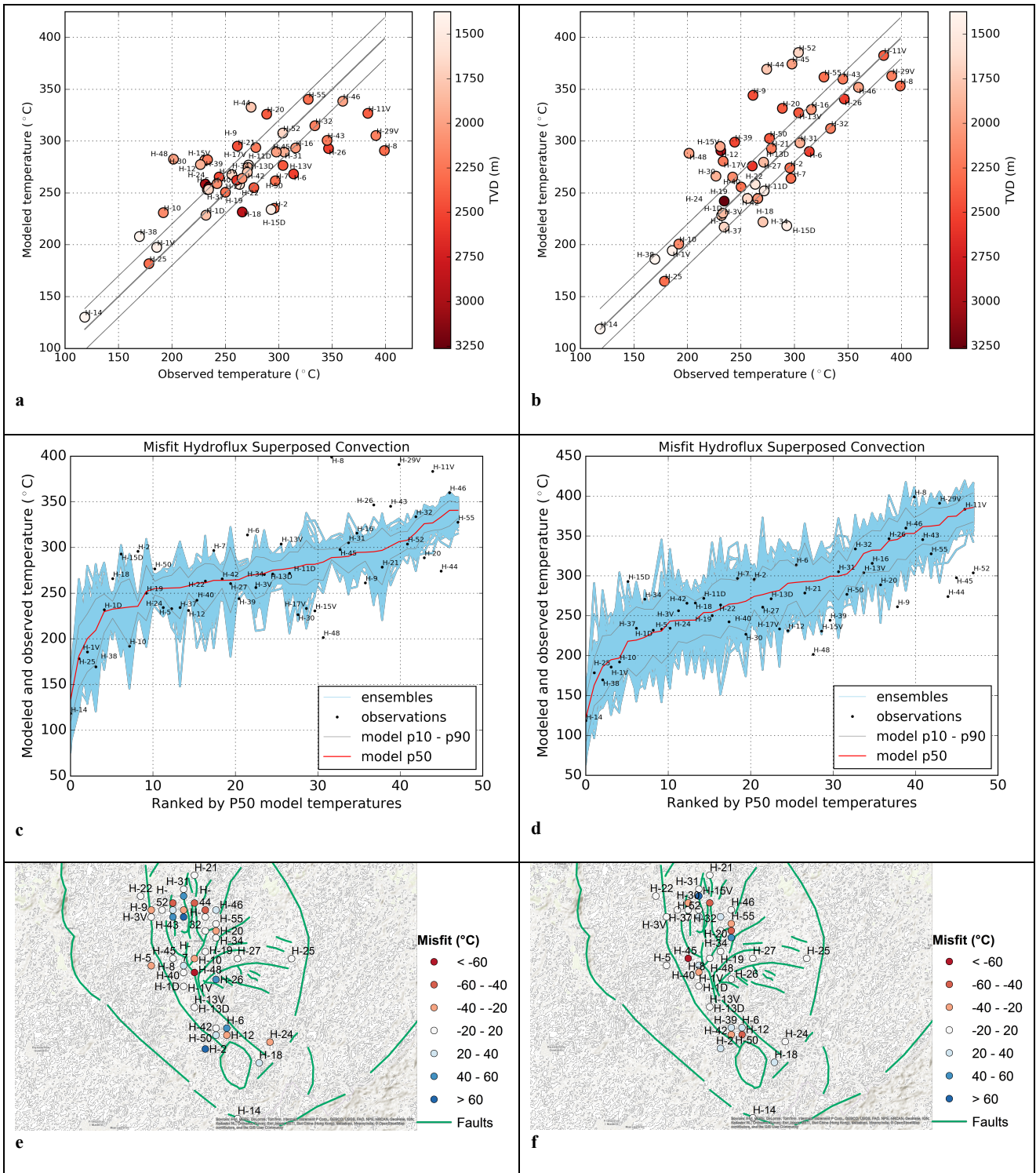


Figure 15: Cross plots of observed and modeled temperature with depth of the measurements (top) and rank plots of modeled temperature (lines) and observed temperatures (dots) at the well locations, ranked by the modeled P50 values of temperature at the well locations (middle). At the bottom misfit (observed minus modeled temperatures). Red colors show a model overestimation of the temperature at the well location, while blue colors show an underestimation. On the left, model D (a, c, and e) and on the right, model E (b, d, and f).

3 Regional temperature structure of Acoculco

3.1 Data

3.1.1 Temperature

The Comision Federal de Electricidad (CFE) drilled two exploratory wells not too far from each other in the area of Acoculco caldera: the well EAC-1 in 1995 and the well EAC-2 in 2008 reaching a final depth of 1810 and 1900 m, respectively. CFE acquired time-temperature series during the thermal recovery of the boreholes enabling the extrapolation of the static temperatures by the application of the well-known Horner Plot method. When 3 or more time-temperature couples of data were available at the same depth, a linear best fitting method including *a priori* standard errors in temperature ($\pm 1^\circ\text{C}$) and time (± 0.25 hrs) observations has been applied (York et al. 2004). This regression method allowed the estimation of the uncertainties on the extrapolated temperatures. The best straight-lines using the regression of York et al. (2004) gave similar results respect the standard linear regression being the differences as low as 1°C . The average uncertainty on the extrapolated temperatures is of the order of $\pm 9^\circ\text{C}$.

Generally, the thermal logs have a spatial resolution of 200 m down to 1000 m and of 50 m from 1000 m down to the bottom hole. At each measurement point, 4 temperatures have been recorded after shut-in times of 6 hrs, 12 hrs, 18 hrs and 24 hrs. In the EAC-1 well additional measurements taken after 288 and 312 hrs (12 and 13 days, respectively) were also recorded at fewer points. In the upper section of both the wells, approximately 1000 m thick, the recorded time-temperature series suddenly decrease as function of increasing shut-in time. This time-dependent trend can be related with the thermal effect of the circulating drilling mud that cooled the bottom hole during drilling and then carried out the heat toward the well-head warming the upper section of the borehole. The magnitude of this thermal effect decreases with depth and nearby 800-1000 m vanishes. Below 1000 m the time-temperature series shown a regular growth as function of shut-in time.

In both the wells, the resulting static profiles show common features (Figure 16): i) a mainly conductive heat transport dominates in the underground and ii) the geothermal gradients show an increase nearby 1.75 – 1.80 km increasing from 106 – 117 $^\circ\text{C}/\text{km}$ in the upper section to 275 – 355 $^\circ\text{C}/\text{km}$ in the deeper one.

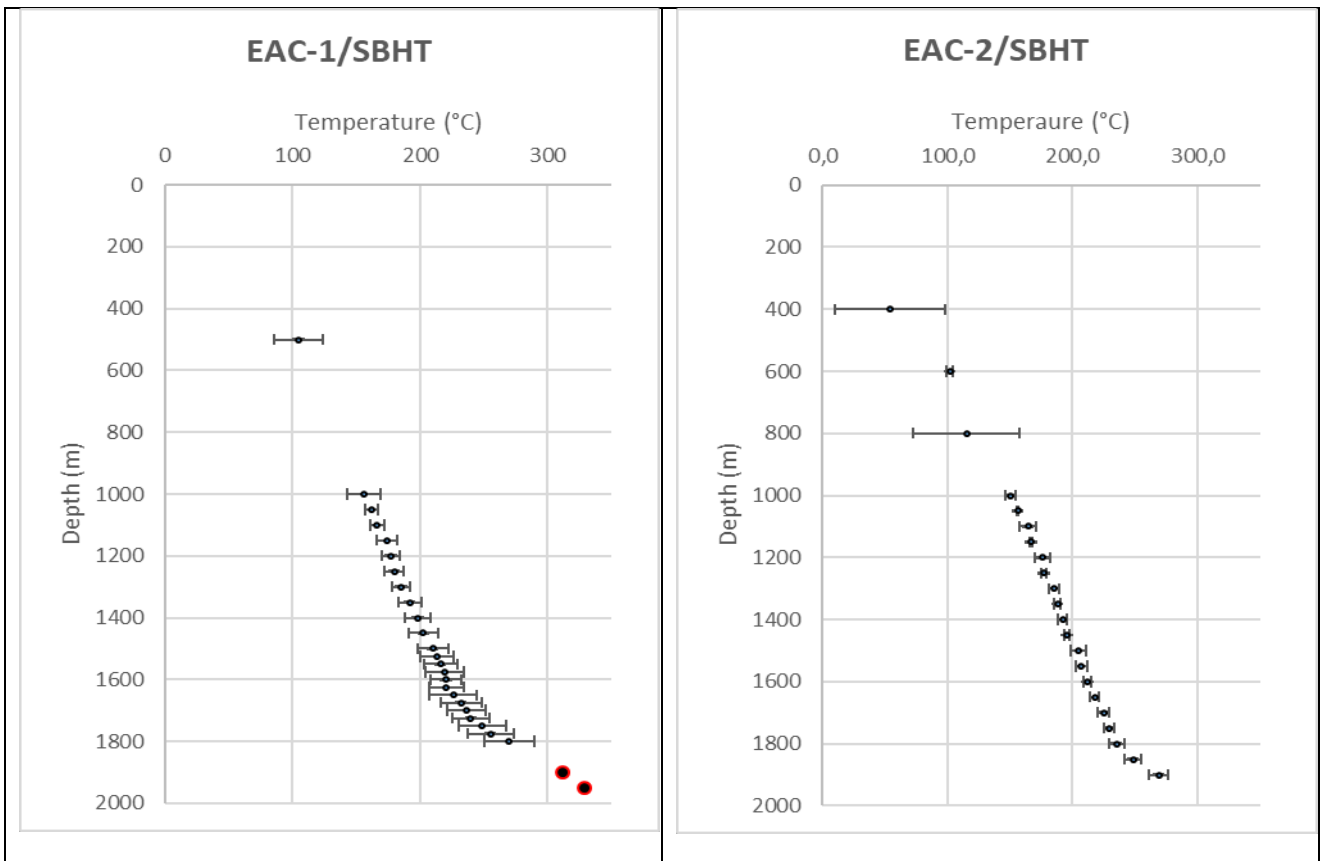


Figure 16: Static temperature profiles with error bars (black dots and bars) of EAC-1 (left) and EAC-2 (right) wells. In EAC-1 well the two deepest temperatures came from the application of the Horner method to 2 time-temperature couples measured after 288 and 312 hrs since the circulation of the drilling mud stops.

3.1.2 Geological model

The Acozulco area was modelled at a regional scale (Fig. 17). For a detailed description of the Acozulco geomodel, please refer to Calcagno et al. (2018).

The geological map from Avellán et al. (2018) is the main references to set up the geomodel. In addition, the Comisión Federal de Electricidad (CFE) has provided a general geological description of two exploration wells. Moreover, other information on the two exploration wells and on the geological setting were retrieved from literature (e.g. López-Hernández et al., 2009; Lorenzo-Pulido et al. 2010). Fieldwork, mainly done by Liotta's team, was also used. A selection of the main faults to be modelled was done. They all have a maximum extension of four kilometres (below ground level) corresponding to the interpretation of the brittle-ductile transition. For the modelling process, the geological formations are described as five groups (see Fig. 17). The Digital Elevation Model (DEM) is provided by INEGI (Instituto Nacional de Estadística Geografía e Informática).

The geomodel at regional scale (56 km x 37 km x 10.5 km, i.e. down to 7 km below sea level) presents five geological groups: basement, granite, skarns, limestones, and volcanics (Fig. 17). The geological map (Avellán et al., 2018) was re-interpreted accordingly.

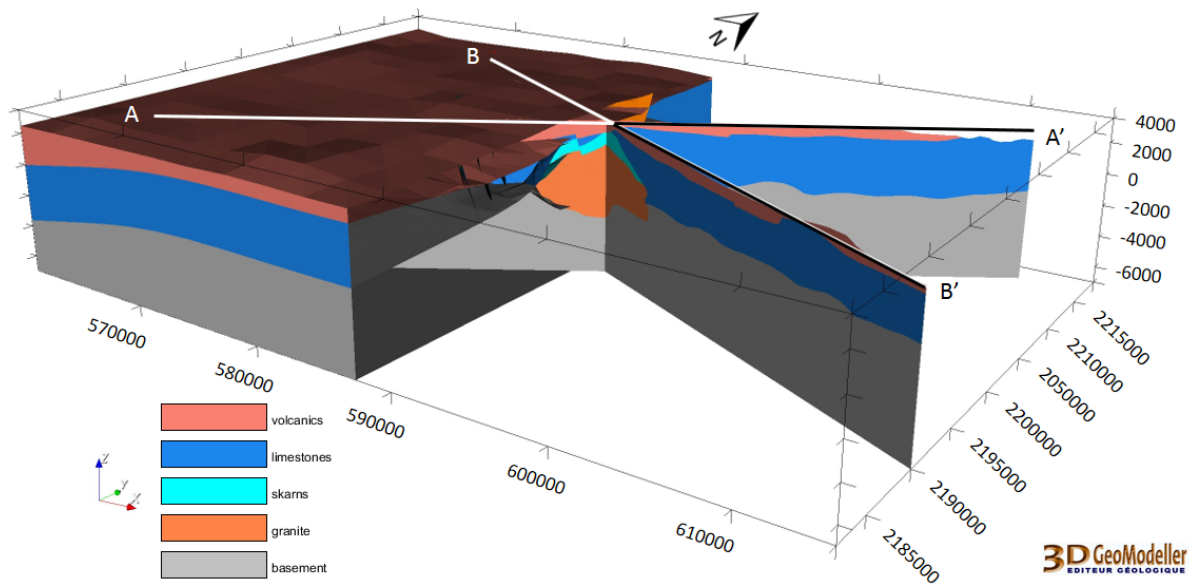


Figure 17: The Acozulco regional geomodel of the five geological groups listed at bottom. Coordinate system is WGS84/UTM zone 14N. Figure taken from Calcagno et al. (2018).

Two geological cross-sections were drawn to interpret the deep structures. They serve as reference for the geological interpretation. Nine complementary cross sections were drawn according to the two references cross-sections to ensure a coherent interpretation, for instance in terms of geological formations thickness.

Acozulco regional geomodel is available on VRE: <https://goo.gl/qYE7xM>.

A local and more detailed geological model is under development in the area of the two exploration wells.

3.2 Methodology

Once a geological model consistent with the available data is made (Task 3.1), it can form the framework of the subsequent regional thermal model. Solving numerical simulations of heat and mass transfer in porous

media is critical in order to assess the geothermal potential (Task 3.2). With the aim to evaluate the regional thermal structure, the concept of lithothermal unit is adopted and the different geological formations were grouped on the basis of their thermal and hydraulic properties. The lithothermal units are treated as a homogeneous and downward anisotropic porous material (Pasquale et al. 2011) in which mixing laws were applied to estimate the effective thermal and hydraulic properties accounting for the in-situ conditions (depth and temperature). The definition of the Acoculco geothermal field considered five fundamental units, from the top to the bottom i) the cap-rock unit, ii) the limestone unit, including the skarn, iii) the basement unit, iv) the old intrusive body and v) the young intrusive body set inside the old one. The thermal properties of the main lithothermal units were assigned from literature data (Canet et al. 2015b) and according to new confidential data released in the framework of Task 6.1. In Table X1a and X1b the physical parameters and the constitutive laws used to describe the macroscopic behaviour of the water-rock system are reported.

The interplay between the gravity and the thermally driven fluid flow is described by the combination of the continuity (Eq. 3.1) and momentum (Eq. 3.2) equations coupled with the energy conservation equation (Eq. 3.3):

$$\rho_w \nabla \cdot \mathbf{u} = 0 \quad (\text{Eq 3.1})$$

$$\rho_w \frac{\partial \mathbf{u}}{\partial t} = -\nabla p + \frac{\mu_w}{\phi} \nabla^2 \mathbf{u} - \frac{\mu_w}{K} \mathbf{u} + \mathbf{F} \quad (\text{Eq 3.2})$$

$$\rho c_r \frac{\partial T}{\partial t} = k_r \nabla^2 T - \rho c_w \mathbf{u} \nabla T + H + Q \quad (\text{Eq 3.3})$$

where \mathbf{u} is the fluid velocity vector (u_x, u_y, u_z), p the pressure, T the temperature, t the time, ρ the density, μ the dynamic viscosity, ϕ the porosity, K the permeability, c the specific heat, k the thermal conductivity, F the volume force accounting for gravity and buoyancy forces acting on the fluid (F_z), H and Q represent the radiogenic heat generation and the magmatic heat source, respectively. The subscripts r and w refer to the rock and water properties, respectively.

The thermal loading released by the magmatic heat source is calculated according to Newton's law of cooling:

$$Q = h \cdot (T_{mag} - T) \quad (\text{Eq 3.4})$$

where h is the convective heat transfer coefficient, T_{mag} the magma emplacement temperature and T the external temperature. The duration of a magmatic event is defined multiplying the heat source term (Eq. 3.4) by an arbitrary pulse function $f(t)$. During the cooling, the release of the latent heat of crystallization (L) is also accounted for by incorporating an effective specific heat (c_{eff}) instead of the true specific heat c for the temperature interval of crystallization (ΔT_m):

$$c_{eff} = c + \frac{L}{\Delta T_m} \quad (\text{Eq 3.5})$$

The time-dependent heat and mass transfer equations (Eqs. 3.1 – 3.3) were solved using the FEM method within a 3-D numerical domain that include a layered crust 10 km thick. As boundary conditions, we applied specific temperature-dependent thermal properties of the rocks, a constant surface temperature, a fixed heat flux at the base of the model and a time-dependent heat flux across the young intrusion boundaries. Not

many heat flow data exist for the area of study, a value of 73 mW/m² is reported in the compilation by Pollak et al (1993). In addition, a new heat flow map of Mexico has been recently published by Prol-Ledesma et al. (2019). Accounting for the radiogenic heat contribution of the upper crustal rocks, a final value of 60 mW/m² was set at the base of the numerical domain.

The regional thermal model was set up with the aim to test the hypothesis about the existence of a recent and relatively shallow magmatic intrusion that induced in the overlaying formations a transient thermal signal. Large computational source allowed to solve the three components of the velocity field, the pressure and the temperature on a mesh grid counting more than 5·10⁶ nodes. We approximated the complex dike and/or laccolite magmatic system with a simpler geometrical shape, i.e. a spheroid. The prolate or oblate spheroid mimics the dike or laccolite ensemble, respectively. Via a Monte Carlo approach, we investigated a number of possible scenarios by varying 1) the emplacement temperature (T_{mag}), 2) the aspect ratio (α), 3) the radius (R) as well as 4) the spheroid depth (Z).

Physical parameter	Symbol	Cap-rock	Limestone	Basement	Old intrusion	Young intrusion
Matrix thermal conductivity	k_{mo} [W/(m K)]					
Heat production	H [μ W/m ³]					
Surface porosity	ϕ_s					
Compaction factor	c [1/km]					
Superficial permeability	K_o [m ²]					
Skin depth	d [m]					
Other constants						
Standard gravity	g [m/s ²]	9.81				
Standard temperature	T_{ref} [°C]	20				
Standard pressure	p_o [Pa]	$\sim 10^5$				
Average soil temperature	T_{av} [°C]	18				
Thermal lapse rate	G_{th} [°C/km]	6.4				
Thermal conductivity correction factors	T_M [°C]	1200				
	k_M [W/(m K)]	1.8418				

Table 3.1: Physical parameters of the lithothermal units

Material	Variable	Constitutive law	Ref
----------	----------	------------------	-----

Water thermal conductivity	$k_w(T)$	polynomial function	
Water density	$\rho_w(T)$	polynomial function	
Water viscosity	$\eta(T)$	polynomial function	
Rock porosity	$\phi(z)$	$\phi(z) = \phi_o \exp(-c \cdot z)$	Pasquale et al. (2011)
Matrix thermal conductivity	$k_m(T)$	$k_m(T) = k_M + \left[\frac{T_{ref} T_M}{T_M - T_{ref}} \cdot (k_{mo} - k_M) \cdot \left(\frac{1}{T} - \frac{1}{T_M} \right) \right]$	Sekiguchi (1984)
Effective thermal conductivity	$k_r(T, z)$	$k_{eff}(T, z) = k_m(T)^{(1-\phi(z))} \cdot k_w(T)^{\phi(z)}$	Pasquale et al. (2011)
Permeability	$K(z)$	$K(z) = K_o \exp(-z/d)$	Ebigbo et al. (2014)

Table 3.2: Constitutive laws used to describe the macroscopic behaviour of the water-rock system

3.3 Result of the thermal model

The Acoculco geothermal system lies within the Tulancingo–Acoculco Caldera Complex (Sosa-Ceballos et al., 2018; López-Hernández et al., 2009) sited in the eastern portion of the Trans-Mexican Volcanic Belt. This volcanic complex formed in the Pliocene time (3.0–2.7 Ma) with the formation of the Tulancingo Caldera. A second event in the Pleistocene time (1.7–0.24 Ma) drove the development of the Acoculco Caldera within the older depression. According with the measured high $3\text{He}/4\text{He}$ values ($R/R_a = 6.3$, Polak et al., 1982) which suggest the presence of an active deep-seated magmatic source, we explained the actual trend of the measured temperature profiles as the shallow expression of a recent magmatic event.

The emplacement depth and temperature as well as the size of the magmatic body are unknown. Our numerical approach consisted in solving the transient heat and mass transport equations in order to forecast the present-day temperature distribution around a hypothetical, and recent magmatic intrusion. The choice of solving for a dominant conductive heat transfer mechanism by setting very low permeability values to the rocks ($K < 10\text{-}18 \text{ m}^2$) is supported by the thermal evidences recorded in the wells and the observed pervasive secondary mineralization both at surface and in the cores that reduced the permeability of the rocks.

We simulated the evolution of the thermal structure as consequence of a fast emplacement of magma at time t_1 having a fixed temperature T_{mag} which persist in the mid-to upper crust until time t_2 . The initial conditions correspond to the steady-state conductive temperature distribution evaluated for a basal heat flow of 60 mW/m^2 . The time-dependent solutions are computed every 1 kyr and the length of the simulation is 155 kyr. The magmatic body starts to warm the overlying rocks as soon as it emplaced at depth. The thermal wave moves upward controlled by the thermal diffusivity structure. The thermal load is provided by the heat source for a time interval of 100 kyr. At time t_2 the heat source starts to cool and the release of the latent heat of crystallization has been considered. The heat source has been parametrized through a Monte Carlo optimization procedure minimizing the misfit between the measured and simulated temperatures.

The normalized root-mean square error (NRMSE) has been computed globally, i.e. using as control points all the 46 borehole temperatures (24 from EAC-1 well and 22 from EAC-2 well). Low NRMSE values are observed in the cooling stage for time larger than 10 kyr. These are related to a better data fitting in the upper section of the thermal profiles but not in the lowermost section where a change in the thermal gradient is observed. The characteristic convex upward trend of the thermal profiles is simulated during the warming phase and as soon as the cooling phase starts. In Figure 18 the thermal profiles evaluated along the EAC-1

well at different times during the warming and cooling phases are shown. As regards the timing, if the heat source is still active and we fall into the warming stage, the thermal wave required about 50-80 kyr to reach the depth of the bottom holes. Instead, if we fall in the cooling stage, the intrusion was active up to about 5-6 kyr ago or less. Choosing the scenarios that give a NRMSE < 4, the emplacement temperature and the top of the intrusion are $850\pm 50^\circ\text{C}$ and 2300 ± 400 m below ground level, respectively. Although a preferred narrow shape of the dikes system gives the better data fitting, we need supplementary boreholes in the area of study or other geophysical data in order to better constrain the lateral extent of the thermal anomaly.

We would stress that as the Acoculco geothermal field has not been yet explored in detail, large uncertainties may exist due to the lack of data. The actual regional model represents the best prediction using the available information from literature and from other GEMex Tasks.

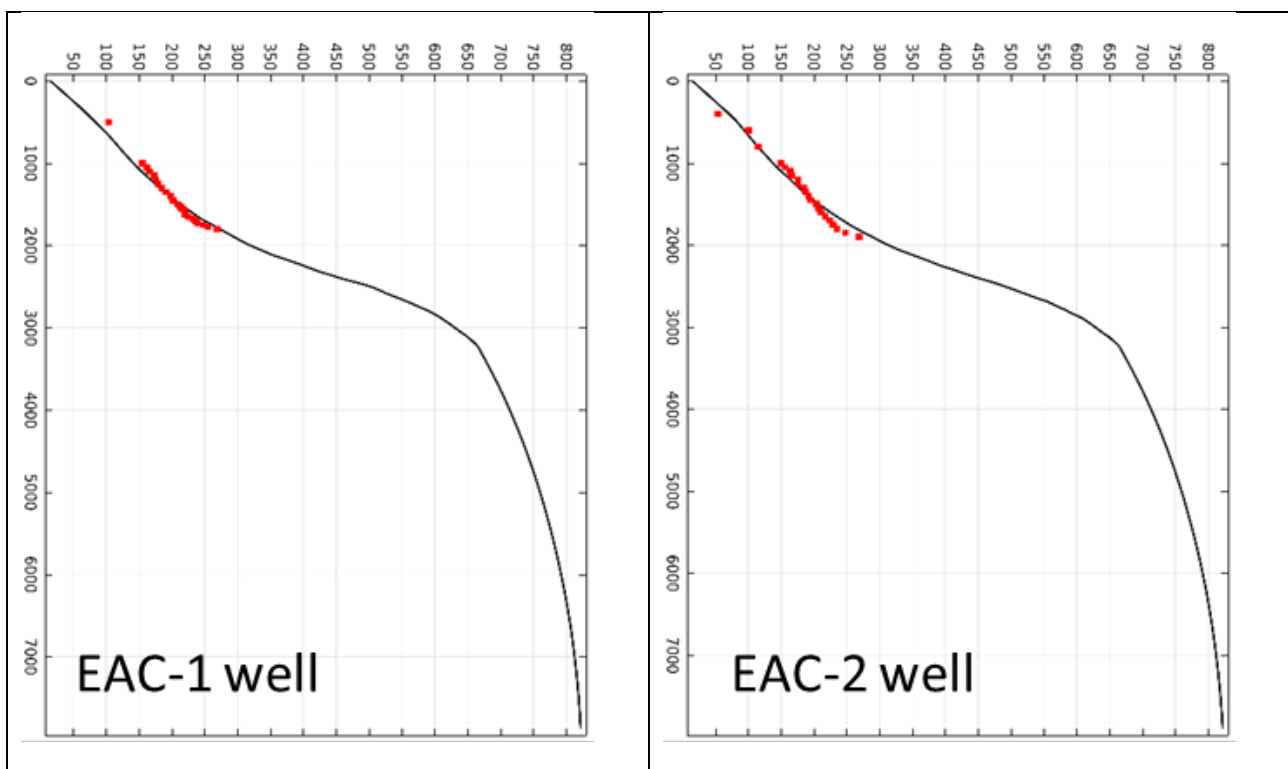


Figure 18: Thermal profiles evaluated as soon as the intrusion starts to cool for an initial emplacement temperature of 850°C and its top set at 2300 m b.g.l.

4 Resource assessment

4.1 Methodology

A volumetric heat-in-place (cf. Muffler and Cataldi, 1978) resource assessment was conducted for both Los Humeros and Acoculco. The main output is the theoretical capacity or heat in place H (J), which is the amount of thermal energy physically present in the reservoir rocks of a certain area or prospect (Fig. XXX). It was decided to not constrain the geothermal potential further into the theoretical (P_{theory}), technical ($P_{technical}$) and economical ($P_{economic}$) potential (MW). Mainly, because of the general lack of data outside the Los Humeros and Acoculco calderas, and in particular because of the lack of data on reservoir conditions in the Acoculco field.

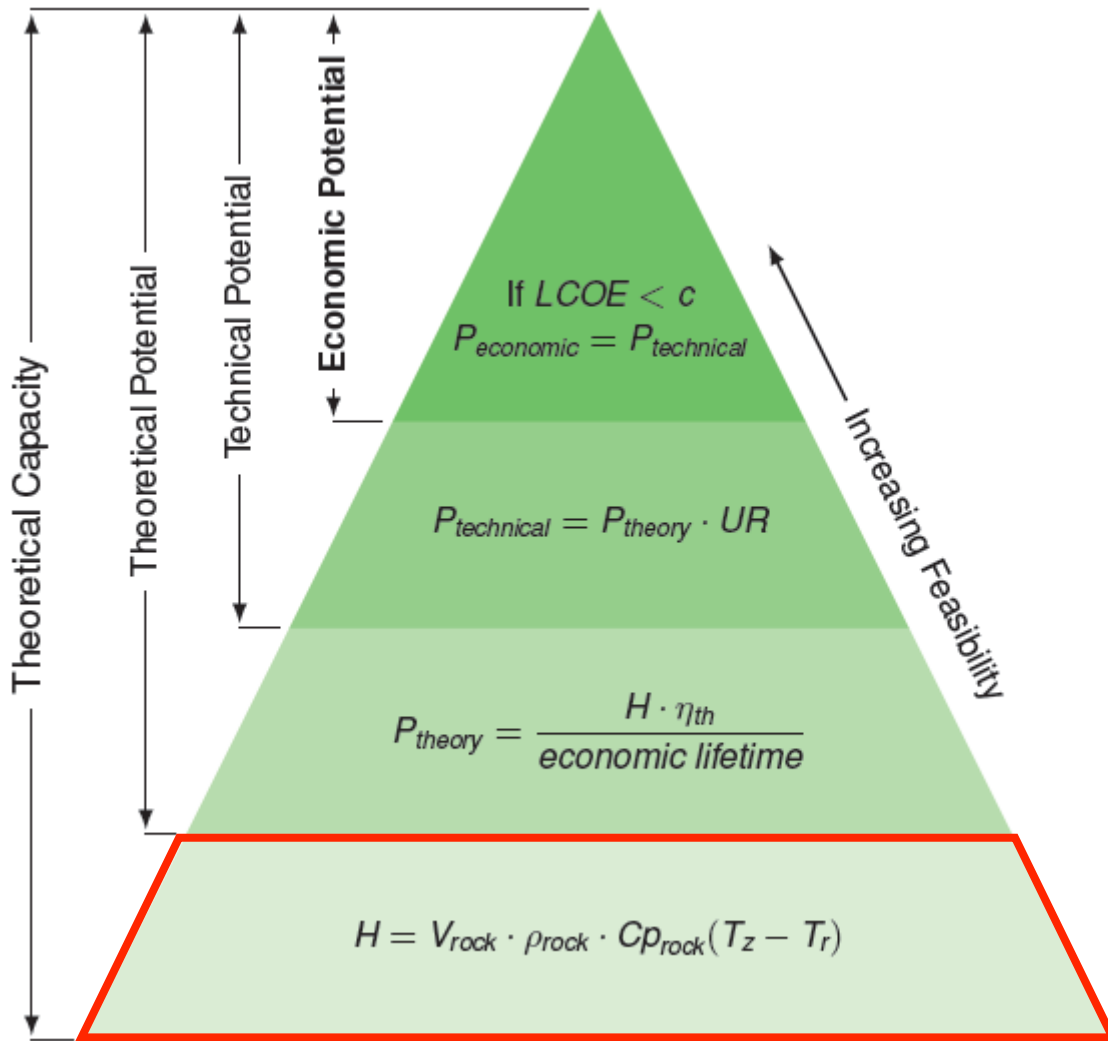
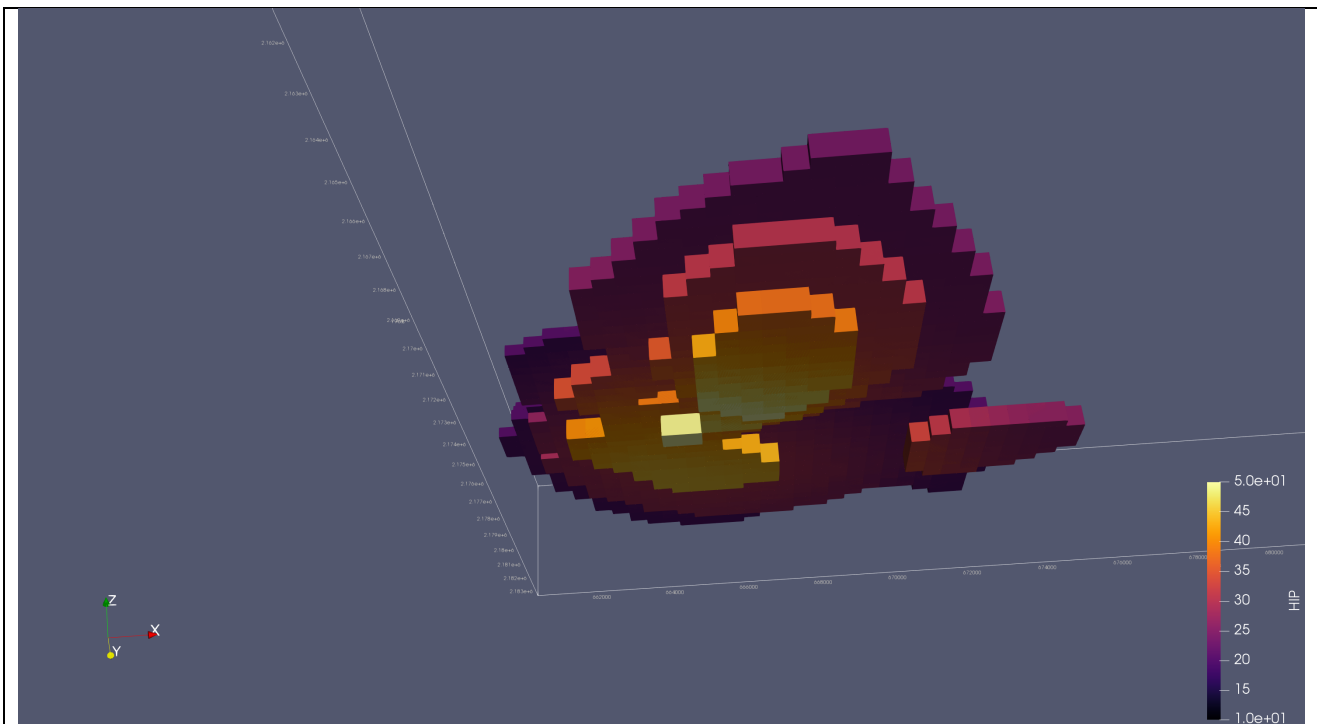


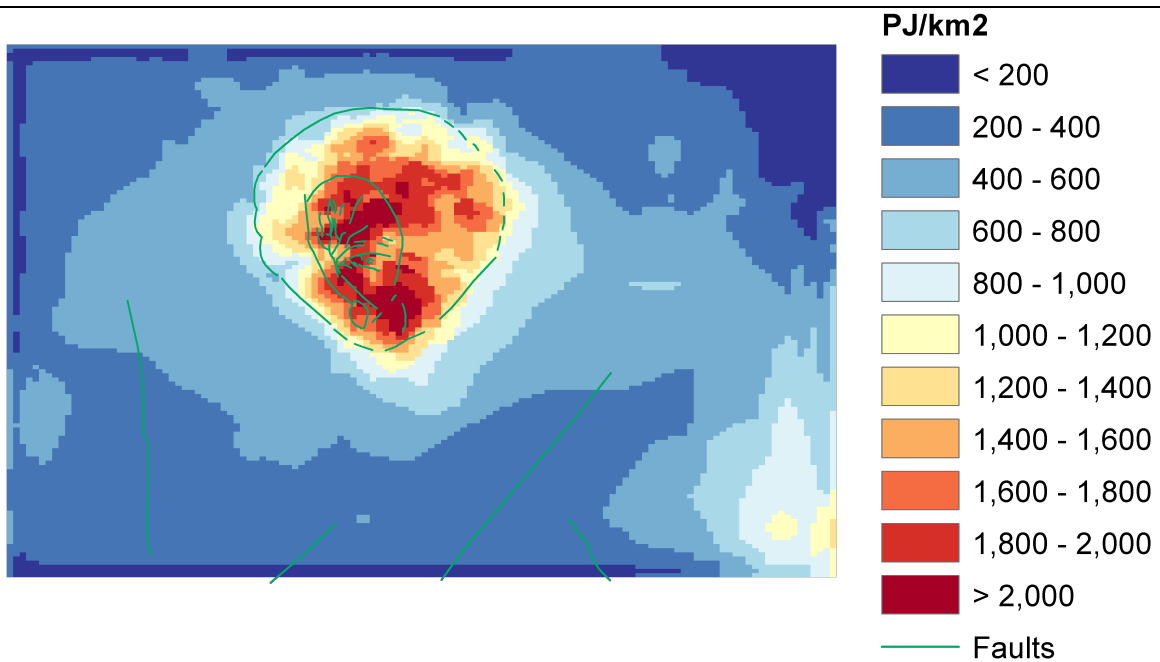
Figure 19: Assessment of the geothermal potential from Limberger et al. (2014). For the Los Humeros and Acochulco fields, the assessment was limited to the Theoretical Capacity (in red). Where H is the heat in place (J), V_{rock} is the rock volume (m^3), ρ_{rock} is the rock density (kg/m^3), $C_{p_{rock}}$ is the specific heat capacity of the rock (J/kg K), T_z is the temperature at depth z ($^{\circ}C$), and T_r is the re-injection temperature ($^{\circ}C$).

4.2 Resource assessment results for Los Humeros

For the volumetric heat-in-place assessment of the Los Humeros region, all layers except the granitic basement (layer 5) were considered as potential reservoir (Table 4.1). The granitic basement is considered to be too deep in the caldera-region to be drilled economically. We adopted a minimum threshold production temperature for T_z of 200 $^{\circ}C$ and we used the surface temperature of 25 $^{\circ}C$ as re-injection temperature T_r . For simplicity, we adopted a single rock density ρ_{rock} of 2600 kg/m^3 and specific heat capacity $C_{p_{rock}}$ of 836 J/kg K. We calculated the stacked potential of all layers above the granite, assuming that all of these layers could potentially be suitable as a reservoir. However, due to the chosen threshold temperature and the general thermal state of the region, the potential will mainly be present in the pre-caldera units of layer 3 and the marble unit of layer 4. We used the temperatures calculated for model D (Section 2.3.2.) as base for this resource assessment. Most of the potential is associated with the high temperatures observed within the caldera zone (Fig. 20). The potential in the SE-corner (Fig. 20b) can be explained by the thermal blanketing effect caused by the relative thick cover of layer 1 and 2 rocks with a very low (<2 W/(m K)) bulk thermal conductivity.



a



b

Figure 20: (a) Bottom view looking in NW-direction of the model cells with a calculated heat-in-place H larger than 10 PJ. (b) Stacked heat-in-place potential H normalized for cell surface area (PJ/km^2), showing the spatial distribution of H and major caldera faults. Most of the potential is associated with the high temperatures inside the caldera. The potential in the SE-corner can be explained by the thermal blanketing effect caused by the relative thick cover of layer 1 and 2 rocks with a very low ($<2 \text{ W}/(\text{mK})$) bulk thermal conductivity.

4.3 Resource assessment results for Acoculco

ThermoGIS code was used to assess the geothermal resources and its potential in the Acoculco area. As geothermal potential the ‘Heat in Place’ was computed for the supposed EGS reservoir. ThermoGIS, which is based on the volume method, was set up with the geological surfaces that limit the reservoir, coming from the 3D regional geological model with a 500 x 500 m² of resolution, the 3D temperature field of the area with 500 x 500 x 100 m³ of resolution and a set of petrophysical rocks properties. The result of the computation is a Heat in Place grid map of the Acoculco area with a 500 x 500 m² as horizontal resolution.

The supposed EGS reservoir in Acoculco is hosted in a volume of rocks including the limestones underlying the volcanites, the skarns and the granite. Consequently, the top limestones surface (Fig. 21a) and the top of the basement surface (Fig. 21b) from the 3D regional geological model were used in the computation. In particular, the top of the basement is a composite surface made of the bottom the limestones and the bottom of the granite. The volume of skarn rocks is included between the two surfaces described.

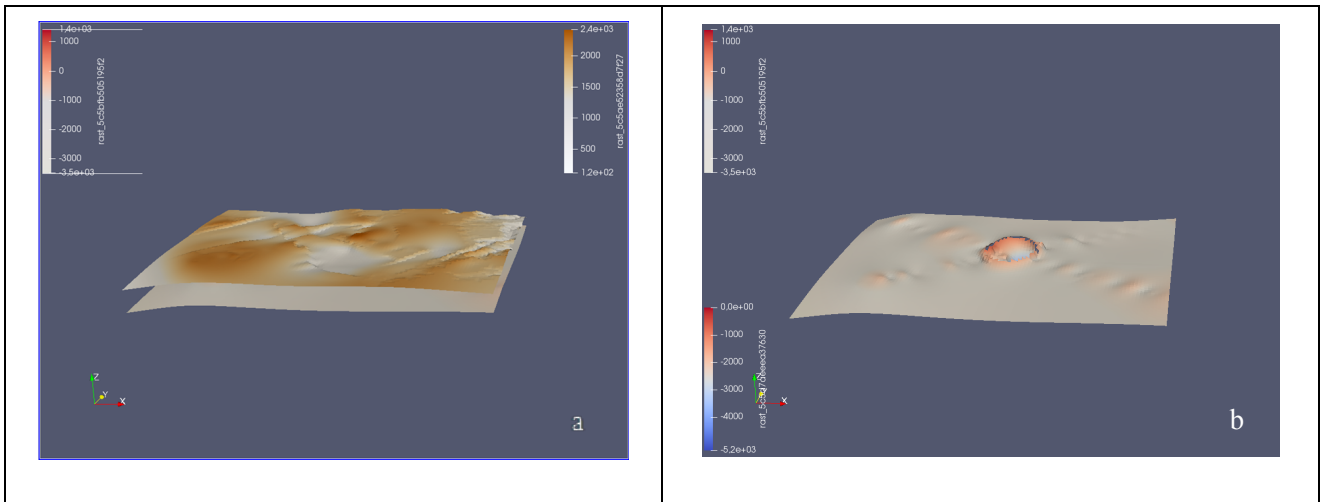


Figure 21: a) top limestone surface; b) top basement surface.

Beside the 3D thermal field, described in section 3, the used petro-physical parameters are reported in table 4.1:

Lithology	Density (kg/m ³)	Specific heat (J/kg K)
Limestones	2600	2650
Granite	836	850

Table 4.1: Petrophysics used values in ThermoGIS runs

Actually to compute the HIP in the supposed EGS reservoir two different runs were executed in two sub-reservoirs, the limestones plus skarns and granites Fig. 22 and Fig. 23.

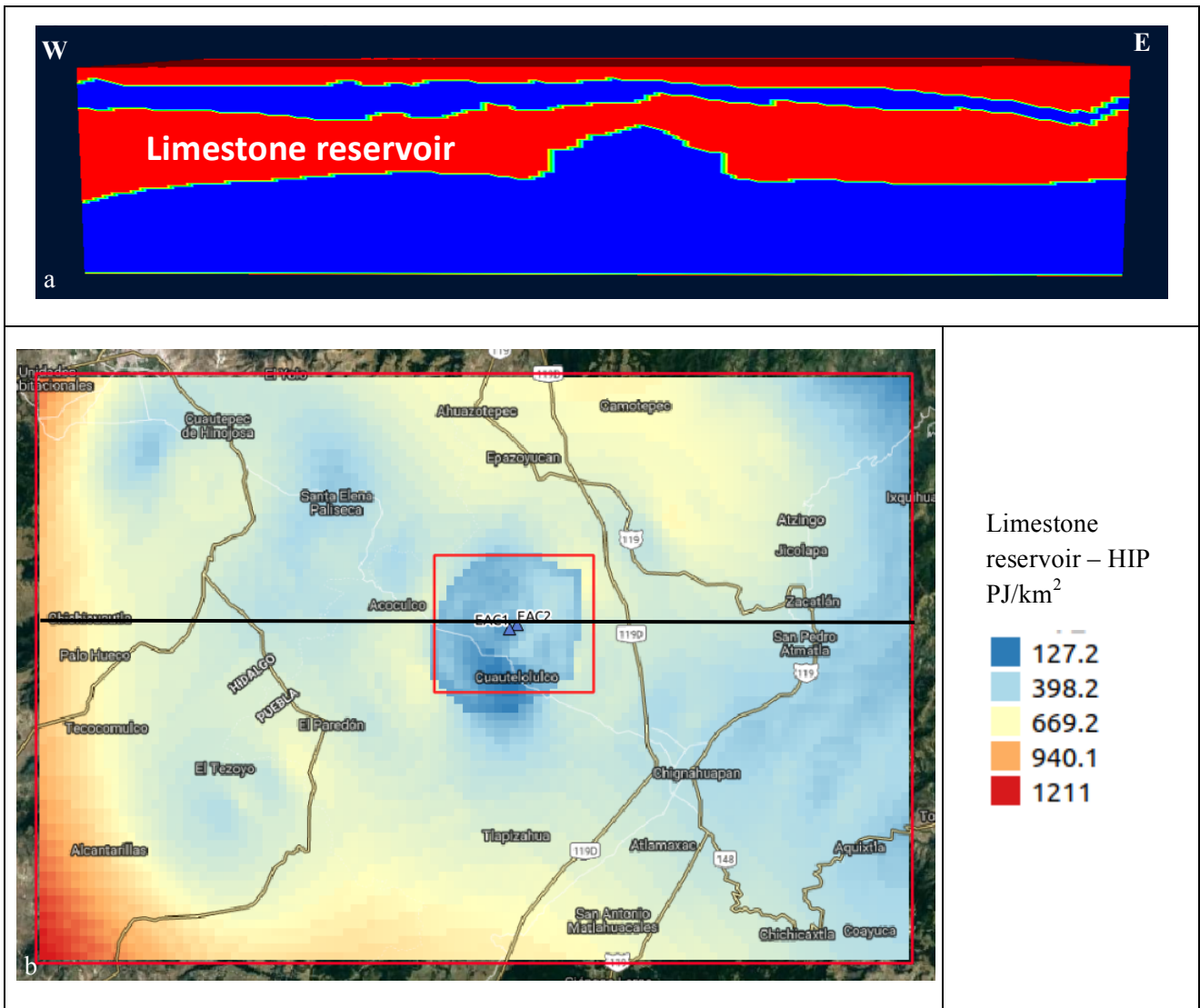


Figure 22: a) cross-section representing the volume of limestones where the HIP was computed; b) HIP map. Large red limit is the regional model boundary. Small red limit is the local geological model boundary. In black the trace of the cross-section reported in the part a of the Figure.

It is worthwhile to remark that although where the heat source is supposed to be and placed in the thermal model (i.e., close to the two exploration wells) the heat stored in the underground is lower than other locations in the map Fig. 22. As for the computation the ‘Volume’ method was applied, the result is affected by the thickness of the reservoir. In the areas of the heat source location, the thickness of the limestones reservoir is limited and consequently the geothermal potential, as HIP, is lower.

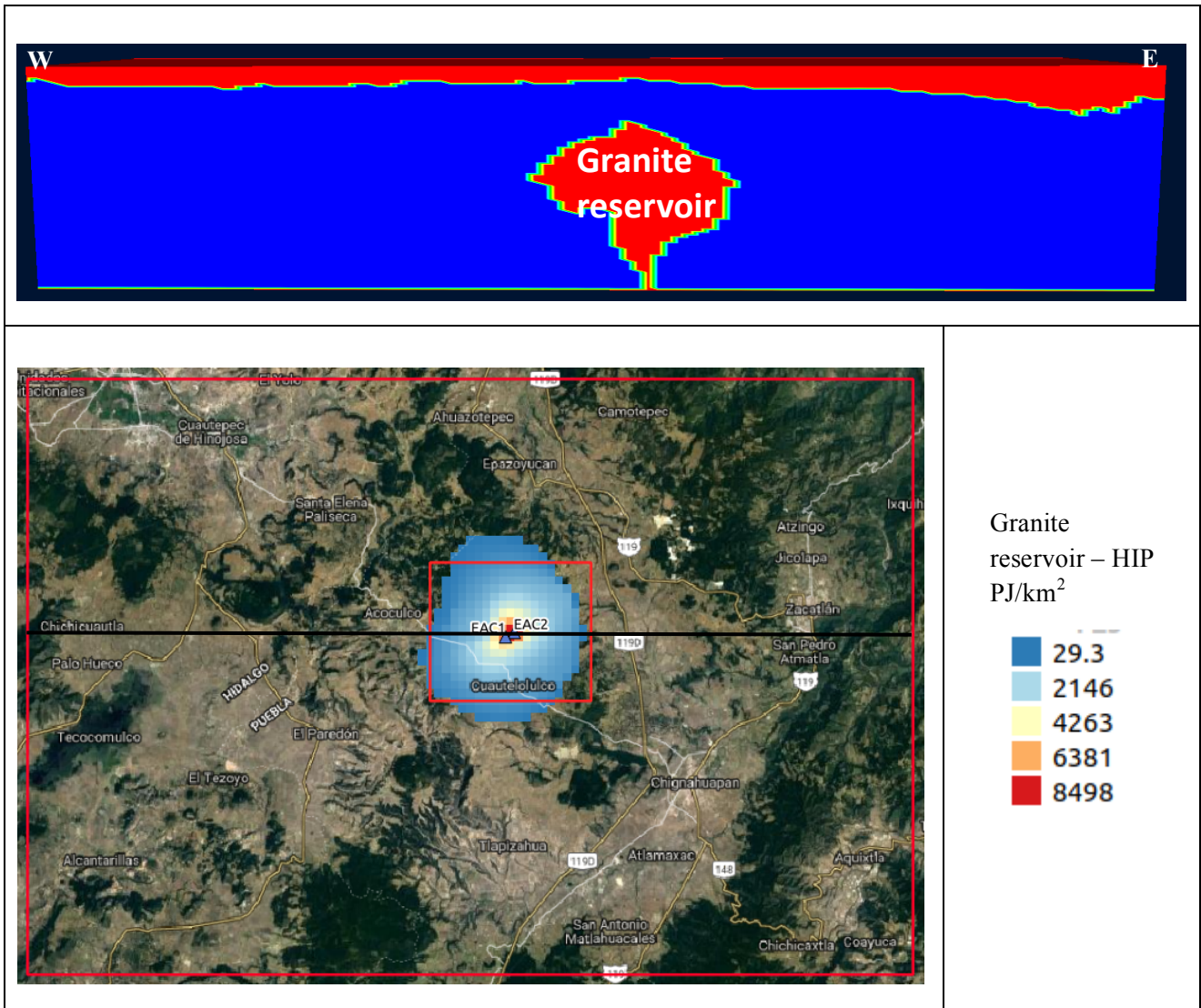


Figure 23: a) cross-section representing the volume of granite where the HIP was computed; b) HIP map. Large red limit is the regional model boundary. Small red limit is the local geological model boundary. In black the trace of the cross-section reported in the part a of the Figure.

To obtain the HIP map on the whole supposed EGS reservoir we computed a simple algebraic sum of the HIP assessed in the two sub-reservoirs. The resulting map is showed in the Fig. 24.

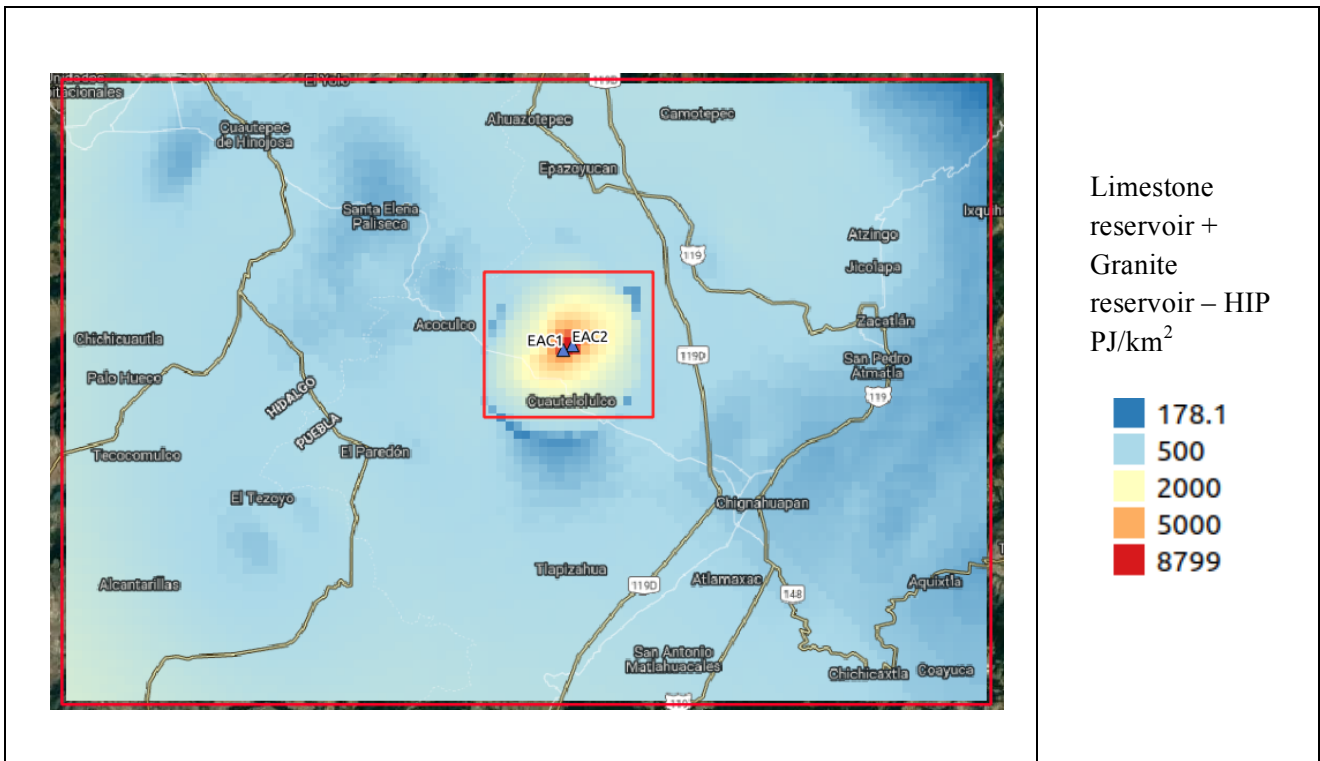


Figure 24: HIP map computed on Limestone plus Granite reservoir. Large red limit is the regional model boundary. Small red limit is the local geological model boundary.

For the studied area (large red boundary) the minimum and maximum value of the heat in place are 178 and 8800 PJ/km² respectively, with a mean values of about 600 PJ/km².

In the area of main interest, within the local geological model sector, the minimum and maximum value of the heat in place are 245 and 8800 PJ/km² respectively, with a mean values of about 1600 PJ/km².

5 Conclusion

The results obtained, both in Los Humeros and Aocolco, outline the present-day thermal structure and provide insight into the thermal evolution, allowing to better characterise deeper and large-scale processes. In Los Humeros, the result of the temperature modelling is very conclusive. The conductive only modelling (Model A) is coherent with the magmatic chamber estimation of Giordano et al. (pers. communication) and Carrasco-Núñez et al. (2018): pancake shaped 9.5 km radius ellipse horizontally and 1.5 km thick at a depth at a depth of 5km. With the hydrogeological system added to the process, the high variability related to advective heat transfer result in an improved fit with the temperature measurements from the wells. In this scenario of a combined magmatic heat source and advective heat transfer, the faults are playing a major role in the localisation of the high temperature zones. A better fit may be achieved by refining the scenarios further and by running higher resolution models. This would enhance the role of the faults which allows to better constrain the rich magmatic history of the Los Humeros Volcanic Complex. Limited data availability for the Aocolco region, has led to a different outcome regarding the thermal structure. The assumption is a deep-seated magmatic source and the modelling has concentrated in explaining the actual trend of the measured temperature profiles as the shallow expression of a recent magmatic event. The period considered is the last 155 kyrs. In case of a still active heat source, 50 to 80 kyr is necessary to reach the well depth and

if the intrusion is at cooling stage then the intrusion was active 5-6 kyr ago. A main outcome about the heat source in Acoculco is that the intrusion is believed to be narrow shape dyke-like with a top at 2300 ± 400 m and $850\pm 50^{\circ}\text{C}$.

The resource assessment has focused on the heat in place. In Los Humeros, only the volcanoclastic sediments and limestone have been considered as exploitable and a threshold production of 200°C has been applied. As a first order assessment all layers are considered as being suitable but the potential is mostly located in the deeper part: pre-caldera unit and marble unit. The stacked heat-in-place show interesting values in the central part as expected but also to the southeast in relation with the blanketing effect of the thick caldera and post-caldera units. In Acoculco, the whole sequence from limestone to volcanic deposits is considered for EGS development but two reservoir options were investigated. For the limestone as a reservoir the thickness of the layer play a predominant role on the result. For the granite as a reservoir, the location of the wells at the centre of the granitic body is the most promising. The combination of the limestone and granite as EGS reservoir point the area of the wells as most interesting.

Both the temperature and heat in place either confirm or define new knowledge or the geothermal areas of Acoculco and Los Humeros. The regional approach allowed, with sometimes little information, to understand what are the main processes and helps characterising these complex systems.

6 References

- Avellán, D. R., Macías, J. L., Layer, P. W., Cisneros, G., Sánchez-Núñez, J. M., Gómez-Vasconcelos, Pola, A., Sosa-Ceballos, G., García-Tenorio, F., Reyes-Agustín, G., Osorio-Ocampo, S., García-Sánchez, L., Mendiola, F., Martí, J., López-Loera, H., and Benowitz, J., 2018. Geology of the Late Pliocene – Pleistocene Acoculco caldera complex, eastern Trans-Mexican Volcanic Belt (México), *J. Maps*.
- Beglinger, S.E., Van Wees, J.-D., Cloetingh, S., and Doust, H., 2012. Tectonic subsidence history and source-rock maturation in the Campos basin, Brazil. *Petrol. Geosci.*, 18 (2), 153-172.
- Calcagno, P., Evanno, G., Trumpy, E., Gutiérrez-Negrín, L. C., Macías, J. L., Carrasco-Núñez, G., and Liotta, D., 2018. Preliminary 3-D geological models of Los Humeros and Acoculco geothermal fields (Mexico) – H2020 GEMex Project, *Adv. Geosci.*, 45, 321-333.
- Canet, C., Hernández-Cruz, B., Jiménez-Franco, A., Pi, T., Peláez, B., Villanueva-Estrada, R. E., Alfonso, P., González-Partida, E., and Salinas, S., 2015a. Combining ammonium mapping and short-wave infrared (SWIR) reflectance spectroscopy to constrain a model of hydrothermal alteration for the Acoculco geothermal zone, Eastern Mexico, *Geothermics*, 53, 154–165.
- Canet, C., Trillaud, F., Prol-Ledesma, R. M., Gonzalez-Hernandez, G., Pelaez, B., Hernandez-Cruz, B., and Sanchez-Cordova, M., 2015b. Thermal history of the Acoculco geothermal system, eastern Mexico: Insights from numerical modeling and radiocarbon dating. *Journal of Volcanology and Geothermal Research*, 305, 56–62.
- Carrasco-Núñez, G., Bernal, J., Dávila, P., Jicha, B., Giordano, G., and Hernández, J., 2018. Reappraisal of Los Humeros Volcanic Complex by New U/Th Zircon and $40\text{Ar}/39\text{Ar}$ Dating: Implications for Greater Geothermal Potential. *Geochem. Geophys. Geosy.*, 19, 132–149.

- Carrasco-Núñez, G., López-Martínez, N., Hernández, J., and Vargas, V., 2017. Subsurface stratigraphy and its correlation with the surficial geology at Los Humeros geothermal field, eastern Trans-Mexican Volcanic Belt. *Geothermics*, 67, 1–17.
- Cherubini, Y., Cacace, M., Scheck-Wenderoth, M., and Noack, V., 2014. Influence of major fault zones on 3-D coupled fluid and heat transport for the Brandenburg region (NE German Basin). *Geoth. Energ. Sci.*, 2, pp. 1-20.
- Cloetingh, S., Van Wees, J. D., Ziegler, P., Lenkey, L., Beekman, F., Tesauro, M., Förster, A., Norden, B., Kaban, M., Hardebol, N., Bonté, D., Genter, A., Guillou-Frottier, L., Voorde, M. T., Sokoutis, D., Willingshofer, E., Cornu, T., and Worum, G., 2010. Lithosphere tectonics and thermo-mechanical properties: An integrated modelling approach for Enhanced Geothermal Systems exploration in Europe. *Earth-Sci. Rev.*, 102, 159–206.
- Emerick, A., and Reynolds, A., 2013. Ensemble smoother with multiple data assimilation, *Comput. Geosci.*, 55, 3–15.
- Evanno G., 2017. Final Dissertation of Master Degree, 3D Preliminary Geological Modelling of the Los Humeros Geothermal Area (Mexico), ENAG/MFE-088-GB-2017.
- Giordano, G., Lucci, F., Rosetti, F., Urbani, S. (in prep.): GEMex Task 3.1 Update on the volcanological conceptual model of Los Humeros geothermal field.
- Goutorbe, B., Lucazeau, F. & Bonneville A., 2007. Comparison of several BHT correction methods: a case study on an Australian data set. *Geophysical Journal International*, 170, 913-922.
- Guillou-Frottier, L., Carré, C., Bourguin, B., Bouchot, V., and Genter, A., 2013. Structure of hydrothermal convection in the Upper Rhine Graben as inferred from corrected temperature data and basin-scale numerical models, *J. Volcanol. Geoth. Res.*, 256, 29–49.
- Hantschel, T. and Kauerauf, A., 2009. *Fundamentals of Basin and Petroleum Systems Modeling*. 978-3540723172, Springer Berlin, Heidelberg, Germany.
- Limberger, P. Calcagno, A. Manzella, E. Trumpy, T. Boxem, M. Pluymaekers, J.-D. van Wees, 2014. Assessing the prospective resource base for enhanced geothermal systems in Europe, *Geothermal Energy Science*, 2, 55–71.
- J. Limberger, J.-D. van Wees, 2013. 3D Subsurface Temperature Model of Europe for Geothermal Exploration. In *Proceedings of the European Geothermal Congress*, Pisa, Italy.
- J. Limberger, J.-D. van Wees, M. Tesauro, J. Smit, D. Bonté, E. Békési, M. Pluymaekers, M. Struijk, M. Vrijlandt, F. Beekman, and S. Cloetingh, 2018. Refining the thermal structure of the European lithosphere by inversion of subsurface temperature data, *Global and Planetary Change*, 171, 18-47.
- López-Hernández, A., García-Estrada, G., Aguirre-Díaz, G., González-Partida, E., Palma-Guzmán, H., and Quijano-León, J. L., 2009. Hydrothermal activity in the Tulancingo–Acoculco Caldera Complex, central Mexico: Exploratory studies, *Geothermics*, 38, 25 279–293.
- Lorenzo-Pulido, C., Armenta-Flores, M., and Ramírez-Silva, G., 2010. Characterization of the Acoculco Geothermal Zone as a HDR System, *GRC Transactions*, 34, 369–372.

- Muffler, P. and Cataldi, C. 1978. Methods for regional assessment of geothermal resources, *Geothermics*, 7, 53-89, 1978.
- Norini, G., Gropelli, G., Sulpizio, R., Carrasco-Núñez, G., Davila-Harris, P., Pellicioli, C., Zucca, F., De Franco, R., 2015. Structural analysis and thermal remote sensing of the Los Humeros Volcanic Complex: implications for volcano structure and geothermal exploration. *J. Volcanol. Geotherm. Res.* 301, 221–237.
- Pasquale, V., Gola, G., Chiozzi, P. and Verdoya, M., 2011. Thermophysical properties of the Po Basin rocks. *Geophysical Journal International*, 186, 69-81.
- Paterson, S., Fowler jr, T., Schmidt, K., Yoshinobu, A., Yuan, E., and Miller, R., 1998. Interpreting magmatic fabric patterns in plutons. *Lithos*, 44, 53–82.
- Polak B.G., Prasalov., E.M, Kononov, V.I., Verkovsky, A.B, González, A., Templos, L.A., Espíndola, J.M., Arellano, J.M, and Manón, A., 1982. Isotopic composition and concentration of inert gases in Mexican hydrothermal systems. *Geofísica Internacional*, 21, 193–227.
- Pollack, H. N., Hurter, S. J., and Johnson, J. R., 1993. Heat- flow from the Earth’s interior—Analysis of the global data set, *Rev. Geophys.*, 31, 267–280.
- ProLedesma, R. M. and Morán-Zenteno, D. J., 2019. Heat flow and geothermal provinces in Mexico. *Geothermics*, 78, 183-200.
- Scheck-Wenderoth, M., Cacace, M., Maystrenko, Y. P., Cherubini, Y., Noack, V., Kaiser, B. O., Sippel, J., and Björn, L., 2014. Models of heat transport in the Central European Basin System: Effective mechanisms at different scales. *Marine and Petroleum Geology*, 55, 315-331.
- Sekiguchi, K., 1984. A method for determining terrestrial heat flow in oil basinal areas. *Tectonophysics*, 103, 67–79.
- Sosa-Ceballos, G., Macías, J. L., Avellán, D. R., Salazar-Hermenegildo, N., and Boijseauneau-López, M. E., 2018. The Acoculco Caldera complex magmas: Genesis, evolution and relation with the Acoculco geothermal system. *Journal of Volcanology and Geothermal Research*, 358, 288–306.
- Spear, F., and Cheney, J., 1993. *Metamorphic Phase Equilibria and Pressure-Temperature-Time Paths*. Mineralogical Society of America, Washington, ISBN 0-939950-34-0.
- Van Wees, J. D., Bergen, F. V., David, P., Nepveu, M., Beekman, F., Cloetingh, S. and Bonté, D., 2009. Probabilistic tectonic heat flow modeling for basin maturation: Assessment method and applications. *Marine and Petroleum Geology*, 26, 536–551.
- Verma, S. and Gómez-Arias, E., 2013. Three-dimensional temperature field simulation of magma chamber in the Los Humeros geothermal field, Puebla, Mexico. *Appl. Therm. Eng.*, 52, 512–515.
- Verma, S., and Gómez-Arias, E., 2014. Optimal discretization time and mesh size in three-dimensional temperature field simulation in two Mexican geothermal fields, Puebla, Mexico. *Geothermics*, 51, 91–102.
- Weydt, L., Bär, K., and Perizonius, J. (Task 6.1): Petrophysical rock properties “Reservoir samples – CFE” – Preliminary results (31.07.2018).

York, D., Evensen, N. M., Martinez, M. L., and Delgado, J. D. B., 2004. Unified equations for the slope, intercept, and standard errors of the best straight line. *Am. J. Phys.*, 72, 367–375.



Coordination Office, GEMex project

Helmholtz-Zentrum Potsdam
Deutsches GeoForschungsZentrum

Telegrafenberg, 14473 Potsdam

Germany